ANNUAL REVIEWS

*Annual Review of Fluid Mechanics*

# Highly Resolved Brownian Motion in Space and in Time

Jianyong Mo and Mark G. Raizen

Center for Nonlinear Dynamics and Department of Physics, The University of Texas at Austin, Austin, Texas 78712, USA; email: raizen@physics.utexas.edu

Annu. Rev. Fluid Mech. 2019.51:403-428. Downloaded from www.annualreviews.org
Access provided by University of Texas - Austin on 01/19/19. For personal use only.

Annu. Rev. Fluid Mech. 2019. 51:403–28

First published as a Review in Advance on September 27, 2018

The *Annual Review of Fluid Mechanics* is online at fluid.annualreviews.org

https://doi.org/10.1146/annurev-fluid-010518-040527

Copyright © 2019 by Annual Reviews.
All rights reserved

ANNUAL REVIEWS CONNECT

www.annualreviews.org

- Download figures
- Navigate cited references
- Keyword search
- Explore related articles
- Share via email or social media

## Keywords

short-timescale Brownian motion, optical tweezers, hydrodynamics, boundary effects, nonequilibrium

## Abstract

Since the discovery of Brownian motion in bulk fluids by Robert Brown in 1827, Brownian motion at long timescales has been extensively studied both theoretically and experimentally for over a century. The theory for short-timescale Brownian motion was also well established in the last century, while experimental studies were not accessible until this decade. This article reviews experimental progress on short-timescale Brownian motion and related applications. The ability to measure instantaneous velocity enables new fundamental tests of statistical mechanics of Brownian particles, such as the Maxwell–Boltzmann velocity distribution and the energy equipartition theorem. In addition, Brownian particles can be used as probes to study boundary effects imposed by a solid wall, wettability at solid–fluid interfaces, and viscoelasticity. We propose future studies of fluid compressibility and nonequilibrium physics using short-duration pulsed lasers. Lastly, we also propose that an optically trapped particle can serve as a new testing ground for nucleation in a supersaturated vapor or a supercooled liquid.

Annu. Rev. Fluid Mech. 2019.51:403-428. Downloaded from www.annualreviews.org
Access provided by University of Texas - Austin on 01/19/19. For personal use only.

# 1. INTRODUCTION

## 1.1. History of Brownian Motion

Brownian motion is the random movement of particles agitated by the thermal motion of the molecules in a fluid. The observation of Brownian motion was first reported in 1785 by Jan Ingenhousz, who was studying the evaporation of liquids under a microscope and observed the "confused, continuous and violent motion" of coal dust on the surface of alcohol (Klafter et al. 1996, p. 33). The Brownian motion of a particle in bulk fluids was first discovered by Robert Brown (1827). Using a simple microscope, he observed the irregular motion in water of pollen as well as inorganic matter like silicified wood and nickel dust. Brown also repeated the experiment after killing the plants and observed the same pollen behavior. Today, this motion is known as Brownian motion. French physicist Louis-Georges Gouy carried out more detailed observations from 1888 to 1895 and found that Brownian motion was more rapid for smaller particles, in less viscous fluids, and at higher temperatures (Duplantier 2006). In 1900, Felix M. Exner made the first quantitative study of Brownian motion by measuring the velocity of Brownian particles suspended in water (Exner 1900). He verified that the measured velocity decreased with increasing particle size and increased with increasing water temperature. However, his results were about three orders of magnitude smaller than those predicted by the energy equipartition theorem (Exner 1900, Kerker 1974).

Louis Bachelier was the first to give a theory of Brownian motion from a random walk perspective in his 1900 thesis "The Theory of Speculation" (Duplantier 2006). In 1905, Albert Einstein explained in precise detail how a microscopic particle is agitated by the thermal motion of fluid molecules based on thermodynamics and Stokes law (Stokes 1850). This explanation of Brownian motion served as a definitive confirmation that atoms and molecules actually exist. Einstein's prediction for the mean squared displacement (MSD) of a free spherical particle in a fluid in one dimension was

$$\langle \Delta x^2(t) \rangle = \langle [x(t+\tau) - x(\tau)]^2 \rangle = 2Dt, \qquad 1.$$

where $D = \frac{RT}{N_A 6\pi\eta a}$ is the diffusion constant and involves Avogadro's constant $N_A$, $R$ is the gas constant, $T$ is the absolute temperature, $\eta$ is the viscosity of the fluid, and $a$ is the radius of the sphere. M. von Smoluchowski (1906) independently derived the expression of MSD in Equation 1 in terms of a random walk, but his result was off by a factor of two. The result in Equation 1 was confirmed experimentally by Jean Perrin (1909), which led to the measurement of Avogadro's number and thus proof of the existence of atoms and molecules. Because of this work, Perrin was awarded the Nobel Prize in Physics in 1926.

The result in Equation 1 is only correct for Brownian motion on long timescales (depending on the particle and fluid properties, typically $\geq$1 ms), conventionally called diffusive Brownian motion. Long-time trajectories of Brownian particles are classic examples of fractals that are continuous everywhere but differentiable nowhere (Vicsek 1992). Therefore, there is no definition for instantaneous velocity in this theory, as the root mean square velocity $\sqrt{\langle v^2 \rangle} = \sqrt{\langle \Delta x^2(t) \rangle}/\Delta t = \sqrt{2D/\Delta t}$ diverges as $\Delta t \to 0$. Einstein knew that his diffusive Brownian motion theory (Einstein 1905) would break down at short timescales. In 1907, he presented the theory that considers the instantaneous velocity of a Brownian particle, in which he provided the timescales at which thermal energy is exchanged between the particle and the fluid, as well as the displacements of the particle during those timescales (Einstein 1907).

In 1908, Paul Langevin proposed a stochastic differential equation to describe Brownian motion, the Langevin equation (Langevin 1908), which was quite different from Einstein's approach and "infinitely more simple" according to him (Lemons & Gythiel 1997, p. 1079). This was the

first mathematical description of the motion of a particle in a fluid over the entire time domain. In Langevin's description, the force on the particle exerted by the fluid is separated into two components, the fluctuation force (also called the thermal force) and the friction force. Both are due to the same physical mechanism, the collisions between the particle and the fluid molecules. They are related by the fluctuation–dissipation theorem (Kubo 1966). Since then, the Langevin model has found broad applications in many fields (Kalmykov & Coffey 2017).

Uhlenbeck & Ornstein (1930) formalized Langevin's approach and extended the results to Brownian motion of a particle in a harmonic potential. The random process that describes the velocity of the Brownian particle is now well known as the Ornstein–Uhlenbeck process, and it predicts an exponential decay long-time tail in the velocity autocorrelation function (VACF). The Ornstein–Uhlenbeck model well describes a particle's Brownian motion in air. However, when a particle changes speed in a dense, viscous liquid, it triggers a dynamic, gradual change in the flow around the particle, and this flow affects the force on the particle at future times. Computer simulations of hard spheres in liquids (Rahman 1964, 1966; Alder & Wainwright 1967, 1970) showed power law behavior for the VACF at long timescales, as opposed to the exponential decay expected from the Ornstein–Uhlenbeck model. Motivated by this discrepancy, Zwanzig & Bixon (1970) and Widom (1971) developed improved models of Brownian motion in liquids that account for fluid dynamic memory effects: The Stokes drag force at any instant depends on the history of the particle's motion, not just the particle's instantaneous velocity. In fact, Stokes (1850) had already derived the result for hydrodynamic friction on an oscillating spherical particle. The same result in the time domain was derived by Boussinesq (1885) and Basset (1888), and the resulting force, which appears as a convolution integral over the past velocities of the particle, is known as the Boussinesq–Basset force. These results lead to the hydrodynamic theory of Brownian motion, which can be used to describe the Brownian motion of a particle in a liquid.

## 1.2. Brief Description of Brownian Motion

To better understand Brownian motion, we consider as an example a 3-μm diameter silica sphere (with density $\rho_p = 2 \times 10^3$ kg/m$^3$) in water ($\rho_f = 10^3$ kg/m$^3$ and viscosity $\eta = 0.9 \times 10^{-3}$ Pa·s) at room temperature. Water is a strongly correlated medium with a mean free path of about a few angstroms, the average distance water molecules can travel between collisions. The collision rate between the microsphere with surrounding water molecules is about $10^{20}$ Hz. Instead of studying Brownian motion at the single collision level, most successful theories (Einstein 1905, von Smoluchowski 1906, Langevin 1908) begin from a statistical point of view by averaging over many collisions in a clever way. A similar situation happens in solid state physics when considering the interaction between a crystal containing Avogadro's number of atoms and electromagnetic waves. Instead of tackling this problem at the single-atom level, people treat the crystal as a collective entity of many atoms with macroscopic properties such as energy bands and a refractive index.

Because of the huge difference (a factor of $10^{12}$) in mass between the silica microsphere ($3 \times 10^{-14}$ kg) and a water molecule ($3 \times 10^{-26}$ kg), the motion of the microsphere can only be changed significantly by a large number of collisions. Therefore, it is natural to study Brownian motion in an averaged manner. One of the key questions is how long one should average the collisions without losing information. The first natural guess is to use the mass ratio factor, that is, to average the motion on the order of $10^{12}$ collisions.

There are two important timescales to consider when averaging collisions in order to correctly describe Brownian motion. One is $\tau_p = m_p/(6\pi\eta a) = (2\rho_p a^2)/(9\eta)$, known as the momentum relaxation time of the particle (Uhlenbeck & Ornstein 1930), where $\rho_p$ is the density of the

Annu. Rev. Fluid Mech. 2019.51:403-428. Downloaded from www.annualreviews.org
Access provided by University of Texas - Austin on 01/19/19. For personal use only.

particle. This indicates how long the particle takes to lose its momentum to the surrounding fluid. $\tau_p$ increases with increasing size and density of the particle and decreases with increasing viscosity of the fluid. The other timescale is $\tau_f = \rho_f a^2/\eta$, the time for vorticity in the fluid to travel one microsphere radius $a$, where $\rho_f$ is the density of the fluid. This directly relates to the hydrodynamic memory effects (Lukic et al. 2005, Franosch et al. 2011). For a 3-μm diameter silica sphere in water, these two timescales are comparable ($\tau_p = 1$ μs and $\tau_f = 2.25$ μs), during which about $10^{14}$ collisions occur. The averaging time interval should be shorter than both $\tau_p$ and $\tau_f$ to fully resolve the momentum relaxation. Thus, the mass ratio ($10^{12}$) between the sphere and a water molecule is indeed a good estimation.

Despite many successful experimental studies of Brownian motion on long timescales, experimental measurements of the instantaneous velocity and thus kinetic energy of the thermal motion of microscopic particles were not possible until recently (Li et al. 2010, Kheifets et al. 2014, Mo et al. 2015a), after many failed attempts (Exner 1900, Kerker 1974). This is because it requires extreme resolution of both time and position. As mentioned above, for a 3-μm diameter silica microsphere in water, the temporal resolution should be shorter than both $\tau_p$ and $\tau_f$. With 2% uncertainty, the temporal resolution needs to be 20 ns. The corresponding spatial resolution is determined by the average displacement, due to Brownian motion, of the microsphere during that time period. At room temperature, the average thermal velocity of the microsphere is about 400 μm/s, resulting in an average displacement of $8 \times 10^{-12}$ m. With 2% uncertainty in the position measurements, the position resolution must be at least $1.6 \times 10^{-13}$ m in 20 ns, corresponding to about $2 \times 10^{-17}$ m/$\sqrt{\text{Hz}}$ in position sensitivity. The position resolution of our experiments is on the level of $10^{-15}$ m/$\sqrt{\text{Hz}}$. Therefore, with current resolution, we cannot resolve the instantaneous velocity of a 3-μm diameter silica microsphere in water with 2% uncertainty.

However, this requirement is reduced to $10^{-15}$ m/$\sqrt{\text{Hz}}$ for a 5-μm barium titanate ($BaTiO_3$; $n = 2.1$, $\rho_B = 4.2 \times 10^3$ kg/m$^3$) microsphere in acetone ($n = 1.35$, $\rho_f = 789$ kg/m$^3$, $\eta = 3.1 \times 10^{-4}$ Pa·s). This is because of two improvements: (*a*) slowing down the dynamics by using acetone (lower viscosity compared to water) and $BaTiO_3$ microspheres (higher density compared to silica) and (*b*) improving signal-to-noise by using $BaTiO_3$ microspheres (a higher refractive index compared to silica improves the scattering efficiency).

## 2. OPTICAL TRAPPING AND BALANCED BEAM DETECTION

Trapping particles (atoms, molecules, ions, nanoparticles, microparticles, biological cells, etc.) is a powerful tool and has revolutionized many fields of science. The experiments described here rely on the use of tightly focused laser beams to both contain and probe the Brownian motion of microspheres in fluids. A dielectric sphere near the focus of a laser beam scatters some of the incident photons in a direction that depends on the particle's position. Changes in the particle's position are encoded in the spatial distribution of the scattered beam, which can be measured with high sensitivity using balanced beam detection. In a balanced beam detection system, the detection beam is typically split into two roughly equal halves. A high-gain balanced detector is typically used to amplify the power difference in the two branches, which has a linear dependence on the position of the trapped particles. Thus, the common-mode noise in the laser beam can be substantially suppressed.

### 2.1. Optical Trapping

Optical trapping relies on momentum exchange between particles and photons. Photons, the discrete quanta of the electromagnetic field, each have a momentum of $p = h/\lambda$. A 1064-nm



Annu. Rev. Fluid Mech. 2019.51:403-428. Downloaded from www.annualreviews.org
Access provided by University of Texas - Austin on 01/19/19. For personal use only.

photon only has a momentum of $6.2 \times 10^{-28}$ kg·m/s. The invention of the laser has made it possible to use the momentum of photons effectively, even though a single photon provides a tiny momentum. For example, 1 W of 1064-nm light, containing about $5 \times 10^{18}$ photons per second, exerts about 7 nN on a totally reflecting mirror at normal incidence. In contrast to incoherent light sources, a laser beam can be tightly focused onto a small particle with a diameter on the order of 1 μm. The radiation force on a 1-μm diameter silica sphere exerted by a 1-W focused laser beam can be $10^4$ times greater than the gravitational force ($3 \times 10^{-13}$ N). Therefore, the optical trap can dominate over the gravitational force in optical tweezer experiments.

Shortly after the laser was invented, Arthur Ashkin (1970) working at Bell labs demonstrated that one could use focused laser beams to accelerate and trap micrometer-sized transparent particles. Ashkin and coworkers also have shown that oil droplets and glass microspheres can be optically levitated in air (Ashkin & Dziedzic 1975) and in vacuum (Ashkin & Dziedzic 1976). In 1986, Ashkin and coworkers observed stable trapping of dielectric particles with the gradient force of a strongly focused laser beam (Ashkin et al. 1986). By then, a powerful tool had been completely developed to trap and manipulate microscopic particles using a tightly focused beam of light, now known as an optical tweezer. This technique soon became a standard tool in many fields (Ashkin & Dziedzic 1987, Ashkin et al. 1987, Ashkin 2000).

The radiation pressure exerted by a laser on a particle can be split into two components: the gradient force and the scattering force. The gradient force is a conservative force, which provides the trapping mechanism, whereas the scattering force is a nonconservative force, which tends to push the particle out of the trap. The total force on the particle is $\mathbf{F}(\mathbf{r}) = \mathbf{F}_{\text{scat}}(\mathbf{r}) + \mathbf{F}_{\text{grad}}(\mathbf{r})$. The scattering force typically only exists in the axial direction of the laser beam and causes a shift of the minimum of the trapping potential in the laser-propagation direction, whereas the gradient force acts in all three dimensions. Thus, there is always a restoring force in the radial direction by a focused beam. The total force on the particle in the axial direction, $F_z = F_z^{\text{scat}} + F_z^{\text{grad}}$, must change sign in order to form a potential minimum in three dimensions. Equivalently, the minimum force in the axial direction, $F_z^{\min} = \min[F_z(\mathbf{r})]$, must be negative if we denote the magnitude of the scattering force as positive. In summary, there are two requirements to stably trap particles. One is the formation of a trap, which requires $F_z^{\min}$ to be negative. The second is that the trap has to be deep enough to withstand thermal fluctuations. The trap depth typically needs to be 10 times greater than the average kinetic energy of the particle. This is due to the fact that the kinetic energy of a particle follows the Maxwell–Boltzmann distribution (MBD) at thermal equilibrium. The particle's instantaneous kinetic energy is significantly likely to be much higher than its average kinetic energy.

Depending on the ratio between the particle size and the trapping laser beam wavelength, the interaction between a microscopic particle and a laser beam is commonly divided into three regimes: the ray optics regime ($D \gg \lambda_0$, where $D$ is the diameter of the particle and $\lambda_0$ is the wavelength of the laser in vacuum) (Ashkin 1992), the Lorentz–Mie regime ($D \sim \lambda_0$) (Nieminen et al. 2007), and the Rayleigh regime ($D \ll \lambda_0$) (Harada & Asakura 1996).

In most optical tweezer experiments, the sizes of the dielectric particles of interest are comparable to the wavelength of the trapping laser ($D \sim \lambda_0$). For instance, in our experiments, the trapping laser beam wavelength was 1064 nm, and the diameters of the microspheres we used typically were between 3 μm and 6 μm. Therefore, neither ray optics nor the Rayleigh approximation is appropriate. For optical trapping of homogeneous and isotropic microspheres, one can use the generalized Lorenz–Mie theory. The mathematical calculation of the generalized Lorenz–Mie theory is quite complex. Here we will only use the computational toolbox developed by T.A. Nieminen et al. (2007) to obtain some numerical results of the optical forces on a microsphere. This computational tool uses spherical partial wave expansion to characterize scattering fields.

Annu. Rev. Fluid Mech. 2019.51:403-428. Downloaded from www.annualreviews.org
Access provided by University of Texas - Austin on 01/19/19. For personal use only.

Annu. Rev. Fluid Mech. 2019.51:403-428. Downloaded from www.annualreviews.org
Access provided by University of Texas - Austin on 01/19/19. For personal use only.

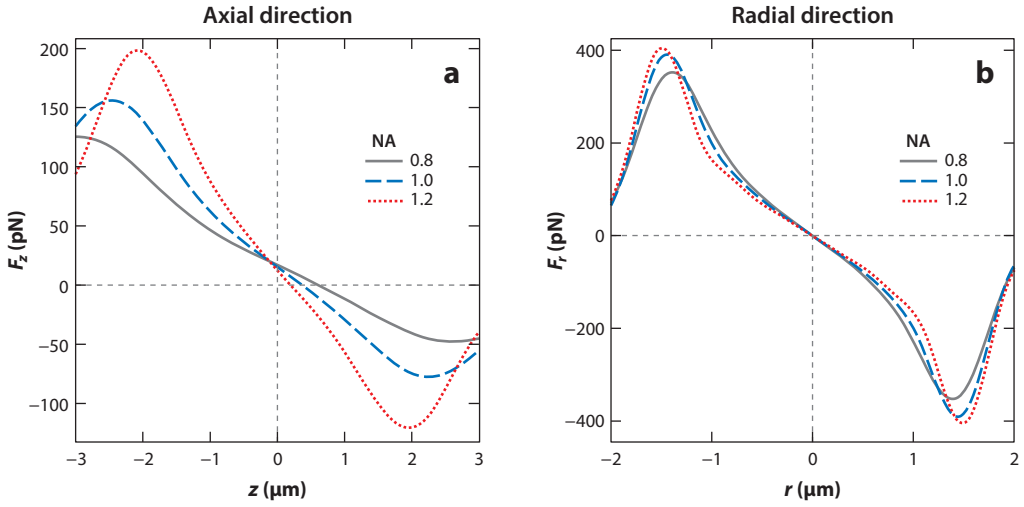


**Figure 1**

Optical forces exerted by a 400-mW, 1064-nm laser beam on a 3-μm diameter silica microsphere in water with different numerical apertures (NA). (*a*) In the axial direction, trapping strongly depends on NA. (*b*) In the radial direction, trapping weakly depends on NA.

**Figure 1** shows the calculated total optical forces on a 3-μm diameter silica microsphere in water in both the axial and radial directions exerted by a 1064-nm, 400-mW laser beam focused by objective lenses with three different numerical apertures (NA): 0.8, 1.0, and 1.2. A trap is formed for all three values of NA, since the total forces change sign in both the axial and radial directions. The optical forces along the radial direction are similar for all three values of NA, as shown in **Figure 1*b***. On the other hand, the optical forces along the axial direction highly depend on NA, as shown in **Figure 1*a***. This is because the scattering force is only along the axial direction. The scattering force shifts the trapping center position in the laser beam propagation direction. It is worth noting that the trap depth and stiffness increase with increasing NA.

**Figure 2** shows the calculated total optical forces, in both the axial and radial directions, exerted on silica microspheres of three different sizes in water by a 400-mW, 1064-nm laser beam focused by an objective lens with NA = 1.0. The optical forces in the axial and radial directions have a similar dependence on the size of microspheres. These calculations show that the larger the size of the microsphere, the deeper the trap. However, it is worth noting that this is not always true, as shown in **Figure 3**. It is interesting that the trap stiffness does not have a monotonic dependence on the size of microspheres.

**Figure 3** shows the minimum axial forces $F_z^{\min}$ on a silica microsphere in water as a function of the size of the microsphere. $F_z^{\min}$ oscillates as the diameter of the microsphere changes. This is due to interference between the scattered light and unscattered light. The oscillation period is about half the wavelength of the laser inside of the microsphere, which is $\lambda_0/(2n_p) = 364$ nm (Li 2011). As discussed before, a trap can only be formed if $F_z^{\min}$ is negative. With NA = 1.0, microspheres with diameters up to at least 8 μm can be trapped because $F_z^{\min}$ is negative. However, with smaller NA (NA = 0.4, 0.5), the trap can only be formed with microspheres of a certain size. This feature may be used as a selection process to size-sort microspheres.

## 2.2. Balanced Beam Detection

A position-sensitive detection system is needed to measure Brownian motion of particles. Video microscopy probably is the most common and intuitive technique to observe particles' motion.

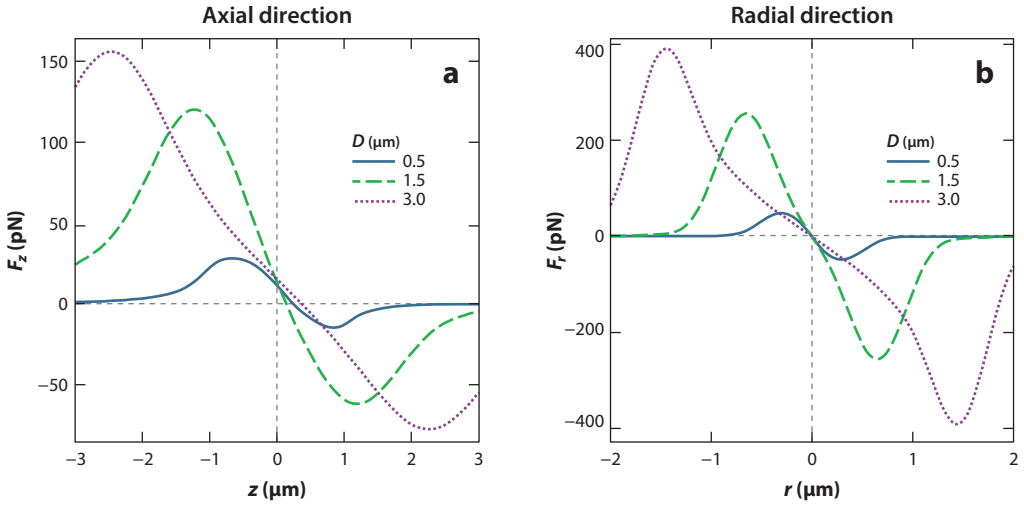


**Figure 2**

Optical forces (*a*) in the axial direction and (*b*) in the radial direction exerted on silica microspheres with different sizes in water by a 400-mW, 1064-nm laser beam with a numerical aperture of 1.0.

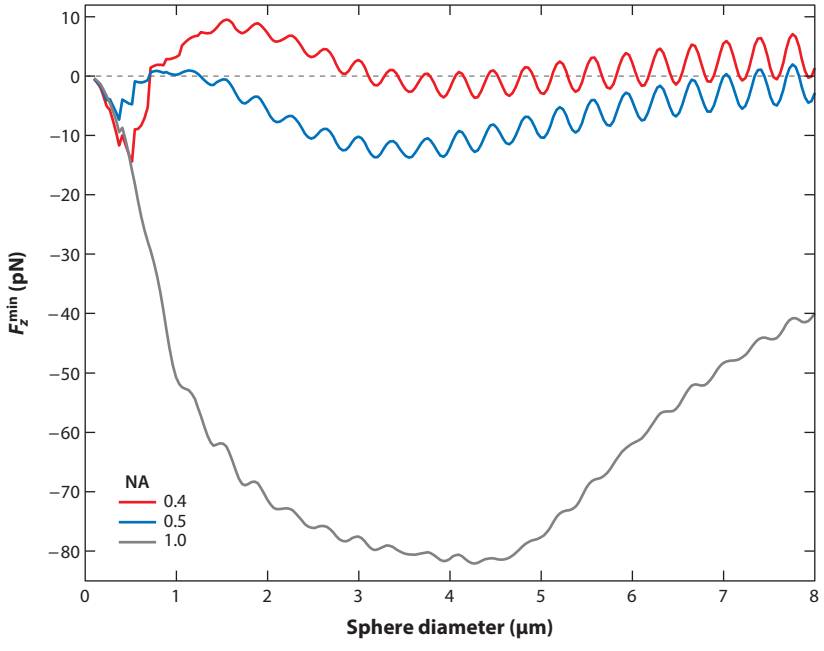


**Figure 3**

The minimum axial forces $F_z^{min}$ exerted on silica microspheres of different sizes in water by a 400-mW, 1064-nm laser beam focused with different numerical apertures (NA).

Annu. Rev. Fluid Mech. 2019.51:403-428. Downloaded from www.annualreviews.org
Access provided by University of Texas - Austin on 01/19/19. For personal use only.

In video microscopy, successive images of one or more particles are taken using cameras, and centroid fitting algorithms are applied to track the particle's position with nanometer resolution, which is much higher than the resolution of the optical microscope itself (Cheezum et al. 2001, Parthasarathy 2012). The bandwidth of video microscopy detection is limited by the frame rate of the camera and illumination intensity, which is typically up to tens of kilohertz (Keen et al. 2007, Hammond & Corwin 2017).

Total internal reflection microscopy is another optical technique that can be used to study Brownian motion. An evanescent wave is generated by a total internal reflection in a plate. A Brownian particle, located near the plate, scatters the evanescent wave differently with different distances to the plate. By measuring the light scattered by the particle, one can determine the separation between particle and plate. The plate is often fixed; thus, the position of the particle in the perpendicular direction can be measured. The technique relies on the rapid exponential decay evanescent wave and achieves ~1-nm spatial resolution and up to ~1-μs temporal resolution (Liu et al. 2014). In addition, this technique is only sensitive to a particle's motion in the perpendicular direction to the plate since the evanescent wave is roughly homogeneous in the transverse direction.

Since the 1990s, balanced beam detection (often also called back-focal-plane interferometry) became the standard tool to measure positions of microscopic particles (Gittes & Schmidt 1998, Pralle et al. 1999, Tolic-Norrelykke et al. 2006, Franosch et al. 2011). Typically, in this detection system, a dielectric particle (often a sphere) is trapped by a focused laser beam and scatters some of the incident photons in a direction that depends on the particle's position. Changes in the particle's position are encoded in the spatial distribution of the scattered beam. The scattered and unscattered light forms the detection beam, which is split into two roughly equal halves. The difference between these two halves is directly related to the position of the particle. This small difference in the two halves can be amplified with high gain, resulting in a high-resolution measurement of the particle's position. In addition, the common-mode noise, such as laser intensity noise, is substantially suppressed because it contributes equally to both halves. The conventional way to split the detection beam and amplify the difference between halves is by using a quadrant detector. However, its detection bandwidth is typically limited to 1 MHz due to the large capacitance of the photodiodes.

A simplified schematic of the balanced beam detection is illustrated in **Figure 4**, in which the detection beam is split into halves by a fiber optic bundle (Chavez et al. 2008) or a D-shape mirror (Li et al. 2010) and focused by two lenses onto two photodiodes of a balanced detector. The photodiodes in the balanced photodetector can be physically separated and have a much

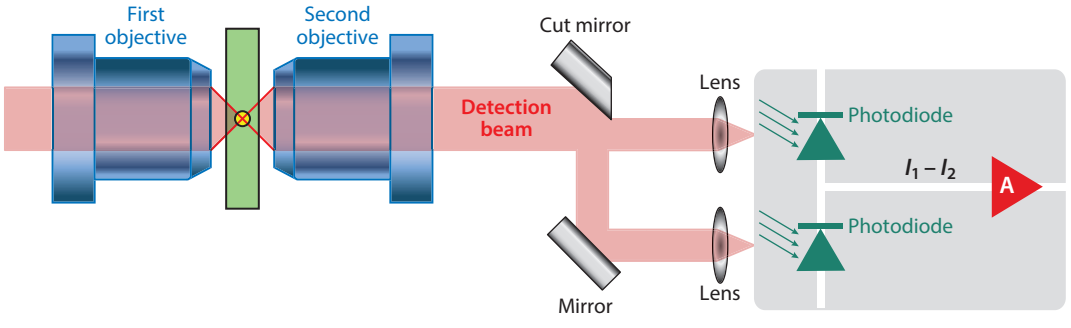


**Figure 4**

Illustration of the balanced detection system. The trapping beam is recollimated by a second objective and split into two roughly equal halves by a cut mirror. Then, the two branches are focused onto two identical photodiodes by two lenses.



Annu. Rev. Fluid Mech. 2019.51:403-428. Downloaded from www.annualreviews.org
Access provided by University of Texas - Austin on 01/19/19. For personal use only.

smaller area than those used in a quadrant detector. Thus, cross talk between two photodiodes is negligible, and the capacitance of the photodiodes can be reduced down to ∼10 pF. Furthermore, the photocurrent from each diode is amplified individually before subtraction in a typical quadrant detector, while the balanced detector photodiodes are wired in a push–pull configuration, and only the difference in photocurrent is amplified. This allows much higher gain, higher bandwidth, and lower noise. Waleed et al. (2017) proposed methods to improve the detection efficiency by filtering out the laser's even spatial modes since particle position information is encoded primarily in the odd spatial modes.

The output voltage signal $V$ of the balanced detector is proportional to the displacement $\Delta$ of the microsphere. The relationship can be written as

$$V = \Gamma P \chi Z \Delta, \qquad 2.$$

where $P$ is the detection beam power, $Z$ is the transimpedance gain of the detector (volts/ampere), $\chi$ is the responsivity of the photodiode (amperes/watt), and $\Gamma$ is the optical gain of a particular system, which has a dimension of inverse length. Based on this, the position sensitivity can be improved by increasing the optical gain, the detection power, the photodiodes' responsivity, and the transimpedance gain. It is worth noting that the detector bandwidth is inversely proportional to the transimpedance gain.

Noise in the Brownian motion measurements includes classical noise (mechanical vibration of the trapping and detection optics, laser intensity noise, laser pointing noise, and electronic noise from the balanced photodetector and acquisition card circuits) and quantum fluctuation noise (shot noise of the laser beam). Typical optical tweezer experiments are limited by classical noise at low frequencies and quantum shot noise at high frequencies. The laser intensity noise, which is the major classical noise source in many experiments, is substantially canceled out because it affects both balanced halves equally. Laser pointing noise can be significantly reduced by fiber coupling the laser into a single-mode fiber. Noise caused by vibration of the optics can be minimized by mounting all of the optics on a vibration-isolation optical table. The fundamental limitation in our experiments is shot noise—the quantum fluctuations in the number of photons that arrive at the balanced detector. The number of photons in a laser beam that arrive at the detector in a certain time interval obeys Poisson statistics,

$$p(n) = \frac{\mu^{-n} e^{-\mu}}{n!}, \qquad 3.$$

with an expected value of $\mu$ and a standard deviation of $\sqrt{\mu}$. A 1064-nm laser beam with a power of 100 mW provides $5 \times 10^{17}$ photons per second on average. The Poisson statistics say that we only know the photon flux per second within $7 \times 10^8$. The absolute photon shot noise scales with $\sqrt{P}$, but the signal scales linearly with $P$; thus, the noise floor in the position signal decreases as $1/\sqrt{P}$. Therefore, the signal-to-noise ratio can be improved by increasing the detection beam power. The maximum power can be limited by technical constraints of generating and detecting a high-power laser beam and by absorption and heating of the trapped particle or fluid. It is worth noting that the balanced beam detection is immune to phase fluctuations, about $1.3 \times 10^{-9}$ radians in this case.

## 3. TESTING THE MAXWELL–BOLTZMANN DISTRIBUTION

The one-dimensional (1D) MBD for the velocities of molecules in an ideal gas in thermal equilibrium is given by

$$f(v) = \sqrt{\frac{m}{2\pi k_B T}} \exp\left(-\frac{mv^2}{2k_B T}\right), \qquad 4.$$



Annu. Rev. Fluid Mech. 2019.51:403-428. Downloaded from www.annualreviews.org
Access provided by University of Texas - Austin on 01/19/19. For personal use only.

where $m$ is mass, $k_B$ is Boltzmann's constant, and $v$ is the velocity (Huang 1987). The energy equipartition theorem, $\frac{1}{2}m\langle v^2\rangle = \frac{1}{2}k_BT$, can be derived from the MBD. The actual velocity distribution in certain systems has been predicted to deviate from the standard MBD due to, for example, particle–particle interactions or relativistic effects (Kelvin 1892, Gould 1971, Gould & Levy 1976, Clayton 1974). Lord Kelvin (1892) proposed a simple thought experiment showing a change in the velocity distribution results by adding an arbitrary potential. Additional deviations from the MBD have been predicted for low-density plasmas (Gould 1971), for interstellar molecular hydrogen (Gould & Levy 1976), and in the solar plasma by measuring neutrino flux (Clayton 1974). In spite of predicted deviations, the MBD still holds as a remarkably robust approximation for most physical systems.

The MBD and the energy equipartition theorem for a microsphere in air have been directly verified by Li et al. (2010). This result is to be expected, since the interaction of a particle with the surrounding air is fairly weak. In the case of a particle in a liquid, it is not so clear due to the strong hydrodynamic coupling whether the MBD and energy equipartition theorem still hold. We reported an accurate test of the MBD and the energy equipartition theorem using a $BaTiO_3$ microsphere in acetone (Mo et al. 2015a). We found that the velocity distribution follows a modified MBD,

$$f(v) = \sqrt{\frac{m^*}{2\pi k_B T}} \exp\left(-\frac{m^* v^2}{2k_B T}\right), \qquad 5.$$

where $m^*$ is the effective mass of the microsphere in liquid, which is the sum of the mass of the microsphere $m_p$ and half of the mass of the displaced liquid $m_f$: $m^* = m_p + \frac{1}{2}m_f$ (Hinch 1975, Zwanzig & Bixon 1975, Pomeau & Piasecki 2017). The liquid adds a virtual mass $\frac{1}{2}m_f$ to the microsphere, since accelerating the microsphere requires a force on both the microsphere and the surrounding liquid. As a result, the energy equipartition theorem also needs to be modified to $\frac{1}{2}m^*\langle(v^*_{rms})^2\rangle = \frac{1}{2}k_BT$.

The apparent conflict between our observation and the equipartition theorem can be resolved by considering the effects of compressibility of the liquid (Zwanzig & Bixon 1975). Below timescales on the order of $\tau_c = a/c$, where $c$ is the speed of sound in the liquid and $a$ is the radius of the microsphere, the compressibility of the liquid cannot be neglected and the velocity variance will approach the energy equipartition theorem.

**Figure 5** shows the normalized velocity distribution for three systems: (*a*) a silica microsphere in water (3.06 ± 0.05 μm diameter, $v^*_{rms} = 327$ μm/s), (*b*) a silica microsphere in acetone (3.98 ± 0.06 μm diameter, $v^*_{rms} = 227$ μm/s), and (*c*) a $BaTiO_3$ microsphere in acetone (5.36 ± 0.06 μm diameter, $v^*_{rms} = 104$ μm/s), calculated from 3.6 billion, 200 million, and 144 million data points, respectively. We observed 78%, 83%, and 100% of the mean kinetic energy predicted by the modified energy equipartition theorem for the three systems, respectively, to which the noise contributes about 4%. The three systems give a trend of approaching the instantaneous velocity measurement, showing the importance of using $BaTiO_3$ microspheres and acetone.

We have shown that the instantaneous velocity of a microsphere in a liquid (a $BaTiO_3$ microsphere in acetone) follows the modified MBD, and thus the modified energy equipartition theorem, over a dynamic range of more than six orders of magnitude in count rate and five standard deviations in velocity (Mo et al. 2015a). Assuming ergodicity (Huang 1987), the same conclusion should also be true for an ensemble of identical particles. Measuring the actual instantaneous velocity in liquid as predicted by the equipartition theorem requires that the temporal resolution be shorter than the timescale of acoustic damping, which is 1.0 ns, 1.7 ns, and 2.3 ns for the three systems, respectively. By using a pulsed laser as the detection beam, one can significantly reduce the shot noise and possibly measure the true instantaneous velocity, which is further



Annu. Rev. Fluid Mech. 2019.51:403-428. Downloaded from www.annualreviews.org
Access provided by University of Texas - Austin on 01/19/19. For personal use only.

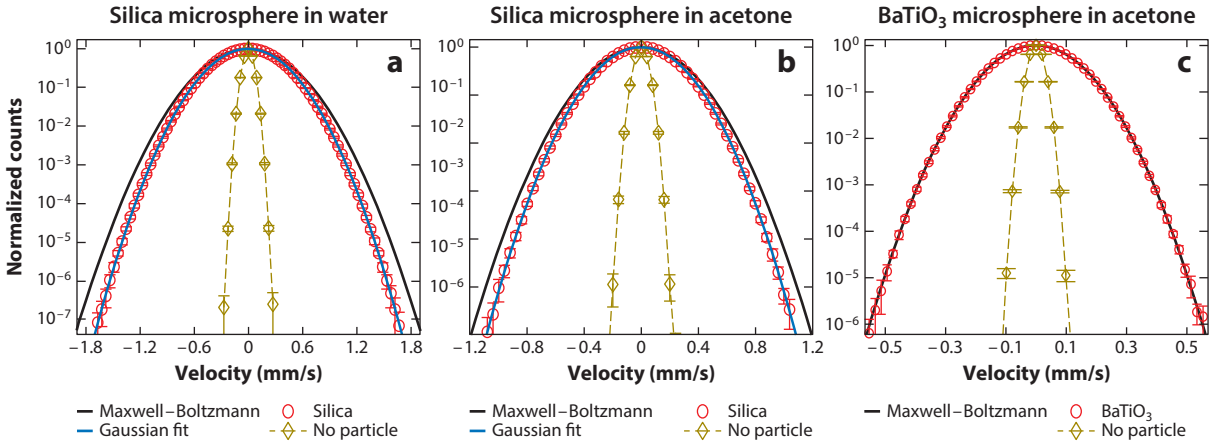


**Figure 5**

The normalized velocity distribution for three systems: (*a*) a silica microsphere in water ($3.06 \pm 0.05$ μm diameter, $v^*_{rms} = 327$ μm/s), (*b*) a silica microsphere in acetone ($3.98 \pm 0.06$ μm diameter, $v^*_{rms} = 227$ μm/s), and (*c*) a barium titanate glass ($BaTiO_3$) microsphere in acetone ($5.36 \pm 0.06$ μm diameter, $v^*_{rms} = 104$ μm/s), calculated from 3.6 billion, 200 million, and 144 million velocity data points, respectively. The histogram bin size for each velocity distribution was set to the root mean squared magnitude of the corresponding noise. Red circles represent the measurements with trapped microspheres, dark yellow diamonds represent the measurements acquired without particles present but with matching detection laser power, black lines are the modified Maxwell–Boltzmann distribution predictions, and blue lines (overlapping almost perfectly with the black line in panel *c*) are Gaussian fits of the measurements, from which the fraction of the mean kinetic energy observed was determined (Mo et al. 2015a).

discussed in Section 6. Our setup can also be used to measure the velocity distribution of a particle in non-Newtonian fluids (Grimm et al. 2011), where deviations from the modified MBD may result from the viscoelasticity of the complex fluid.

## 4. BROWNIAN MOTION NEAR A BOUNDARY

When a particle approaches a boundary, its dynamics will be altered in a way that contains information about the boundary. The boundary effects depend on the particle's shape, orientation, and relative position to the wall; the shape of the wall; and the fluid flow boundary conditions at both the surface of the particle and the wall. Brownian motion of particles near boundaries is relevant to many scientific fields. For instance, in microfluidics, the channel is so narrow that the influence of boundaries is inevitable. Many biological experiments are performed near a glass coverslip. Understanding the influence of boundaries on particle dynamics is of great significance from both a fundamental and an applied point of view.

### 4.1. Anisotropic and Hindered Diffusion of a Microsphere Near a Boundary

It is well known that the mobility of particles decreases as they approach boundaries at which the fluid does not slip. This effect of surface confinement was predicted by Lorentz (1907). The increase of the drag force is attributed to the alteration of the hydrodynamic interaction between the particle and the fluid generated by the no-slip boundaries. This effect is significant when the dimensions of the confining geometry and of the suspended particles are comparable. The motion of the particle becomes anisotropic because the drag force parallel to the wall is typically less than that perpendicular to the wall. The diffusion coefficient of a free particle in bulk fluid is given

Annu. Rev. Fluid Mech. 2019.51:403-428. Downloaded from www.annualreviews.org
Access provided by University of Texas - Austin on 01/19/19. For personal use only.

in Equation 1. The diffusion is hindered when particles are close to boundaries with a no-slip boundary condition.

The system of a spherical particle moving near an infinite flat wall has cylindrical axial symmetry, with an axis through the center of the spherical particle in the direction normal to the wall. Therefore, the particle's motion can be decomposed into parallel and perpendicular directions. The anisotropic and hindered diffusion coefficients of the particle near a no-slip infinite flat boundary in parallel and perpendicular directions are given by Happel & Brenner (1983). Anisotropic diffusion can also be caused by particles' nonspherical shape, where the translational Brownian motion is coupled to rotational Brownian motion, as experimentally demonstrated using digital video microscopy (Han et al. 2006, supporting material). It is worth noting that this work is not highly resolved since it relied on video frame capture (30 frames per second) of Brownian motion. To our best knowledge, highly resolved studies of Brownian motion in space and time have only been conducted to date for spherical particles.

Unlike the case with a sphere near a flat wall, a sphere near a cylindrical wall no longer has cylindrical axial symmetry. The motion of the particle behaves differently in all three directions, $\hat{\mathbf{r}}$, $\hat{\mathbf{z}}$, and $\hat{\boldsymbol{\theta}}$. The anisotropic and hindered diffusion of a point-like sphere outside a no-slip cylinder has been studied previously by Alam et al. (1980). A better approximation can be obtained by adding a geometric series summation for higher-order reflections (Mo 2015), as suggested by Happel & Brenner (1983). The point-like particle approximation used here requires that the radius of the cylinder be much bigger than both the radius of the particle and the sphere–cylinder separation (the distance between the center of the sphere and the surface of the cylinder).

**Figure 6** shows the hindered diffusion coefficients at room temperature of a silica microsphere with diameter 3 μm near a glass cylinder of diameter $80 \pm 1$ μm in the perpendicular direction (normalized to its bulk value, $D_0 = 0.14\ \mu m^2/s$) as a function of sphere–wall separation, from 2.5 μm to 30 μm. The data suggest that the curvature of the cylindrical fiber becomes important when the sphere–wall separation is larger than ∼7 μm.

## 4.2. Boundary Effects on Unsteady Brownian Motion

The effect of a plane wall on the unsteady motion of a sphere in a viscous fluid has been studied by Wakiya (1964) in the parallel direction to the wall and by Gotoh & Kaneda (1981) in the perpendicular direction. These authors showed that the famous power law long-time tail of the VACF in bulk is obliterated by the wall. The first complete theory on boundary effects imposed by a flat wall on Brownian motion over the entire timescale was not available until recently (Felderhof 2005b). However, this work seems inconsistent, and we have proposed modifications to Felderhof's theory (Simha et al. 2018).

The effective inertial mass $m^*$ (which accounts for the inertia of the entrained fluid) of a spherical particle in an unbounded fluid is given by the particle mass $m_p$ plus an added mass of $m_a = m_f/2$, where $m_f$ is the mass of the liquid displaced by the particle: $m^* = m_p + \frac{1}{2}m_f$ (Hinch 1975, Zwanzig & Bixon 1975, Pomeau & Piasecki 2017). The presence of the boundary alters this effective mass, which becomes anisotropic and also depends on the distance to the wall (Mo et al. 2015b, Yang 2010):

$$m^*_\perp = m_p + \frac{1}{2}m_f\left[1 + \frac{3}{8}\left(\frac{a}{h}\right)^3\right], \quad 6.$$

$$m^*_\parallel = m_p + \frac{1}{2}m_f\left[1 + \frac{3}{16}\left(\frac{a}{h}\right)^3\right]. \quad 7.$$



Annu. Rev. Fluid Mech. 2019.51:403-428. Downloaded from www.annualreviews.org
Access provided by University of Texas - Austin on 01/19/19. For personal use only.

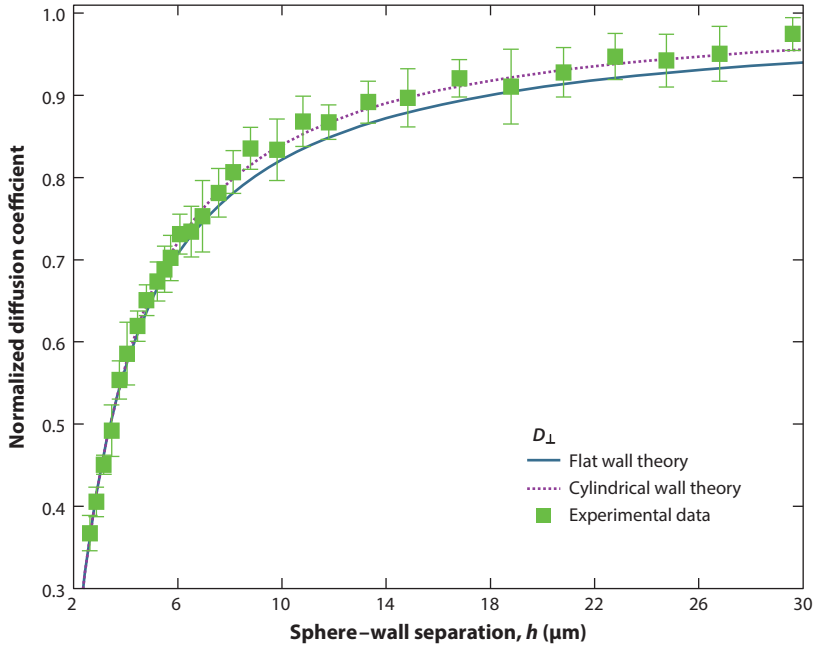


**Figure 6**

The hindered diffusion coefficient measurements (normalized to its bulk value, $D_0 = 0.14\ \mu m^2/s$) of a silica microsphere of $3 \pm 0.1$ μm diameter near a glass cylinder of $80 \pm 1$ μm diameter with a sphere–wall separation $h$ ranging from 2.5 μm to 30 μm. The blue line is the flat wall theory (Happel & Brenner 1983, chapter 7, equation 4.38), the purple dotted line is the cylindrical wall theory (Mo 2015, equation 5.5), and the green squares with error bars represent the experimental data and statistical errors obtained by averaging from 10 measurements at each position.

In addition to surface confinement, it has been reported that the presence of a no-slip boundary also affects the VACF (Jeney et al. 2008, Franosch & Jeney 2009). The long-time tail of the VACF in the bulk case (Alder & Wainwright 1967, 1970) is largely canceled by reflected flow from the wall, resulting in a more rapidly decaying VACF. **Figure 7** shows the VACFs at four positions (with sphere–wall separations $h$ of 30 μm, 6.1 μm, 4.6 μm, and 3.1 μm, respectively) in the perpendicular direction to the wall. The VACFs are normalized to $\langle (v_\perp^*)^2 \rangle = k_B T / m_\perp^*$. The boundary effects are negligible with a large sphere–wall separation of 30 μm, as shown in **Figure 7*a***. **Figure 7*b–d*** shows that the VACF of a particle near a boundary decreases faster as the sphere–wall separation decreases. The rapid decay of the VACF reflects the loss of fluid momentum at the no-slip boundary, which is consistent with previous numerical simulations (Tatsumi & Yamamoto 2013, Huang & Szlufarska 2015, Yu et al. 2015).

In the Einstein–Ornstein–Uhlenbeck model of Brownian motion (Uhlenbeck & Ornstein 1930), which is valid only when the inertia of the fluid is negligible, the corresponding thermal force is white noise, with the flat (one-sided) spectrum $S_F = 4k_B T \gamma_s$. Adding the Basset force to the Einstein–Ornstein–Uhlenbeck model results in the colored thermal force power spectral density (FPSD), $S_F = 4k_B T\, \gamma_s(1 + \sqrt{\omega \tau_f / 2})$, on a particle in an unbounded fluid (Clercx & Schram 1992). This has been experimentally verified (Franosch et al. 2011, Kheifets et al. 2014). Simha et al. (2018) provided the detailed theory for the boundary effects on Brownian motion for the entire timescale.

Annu. Rev. Fluid Mech. 2019.51:403-428. Downloaded from www.annualreviews.org
Access provided by University of Texas - Austin on 01/19/19. For personal use only.

Annu. Rev. Fluid Mech. 2019.51:403-428. Downloaded from www.annualreviews.org
Access provided by University of Texas - Austin on 01/19/19. For personal use only.

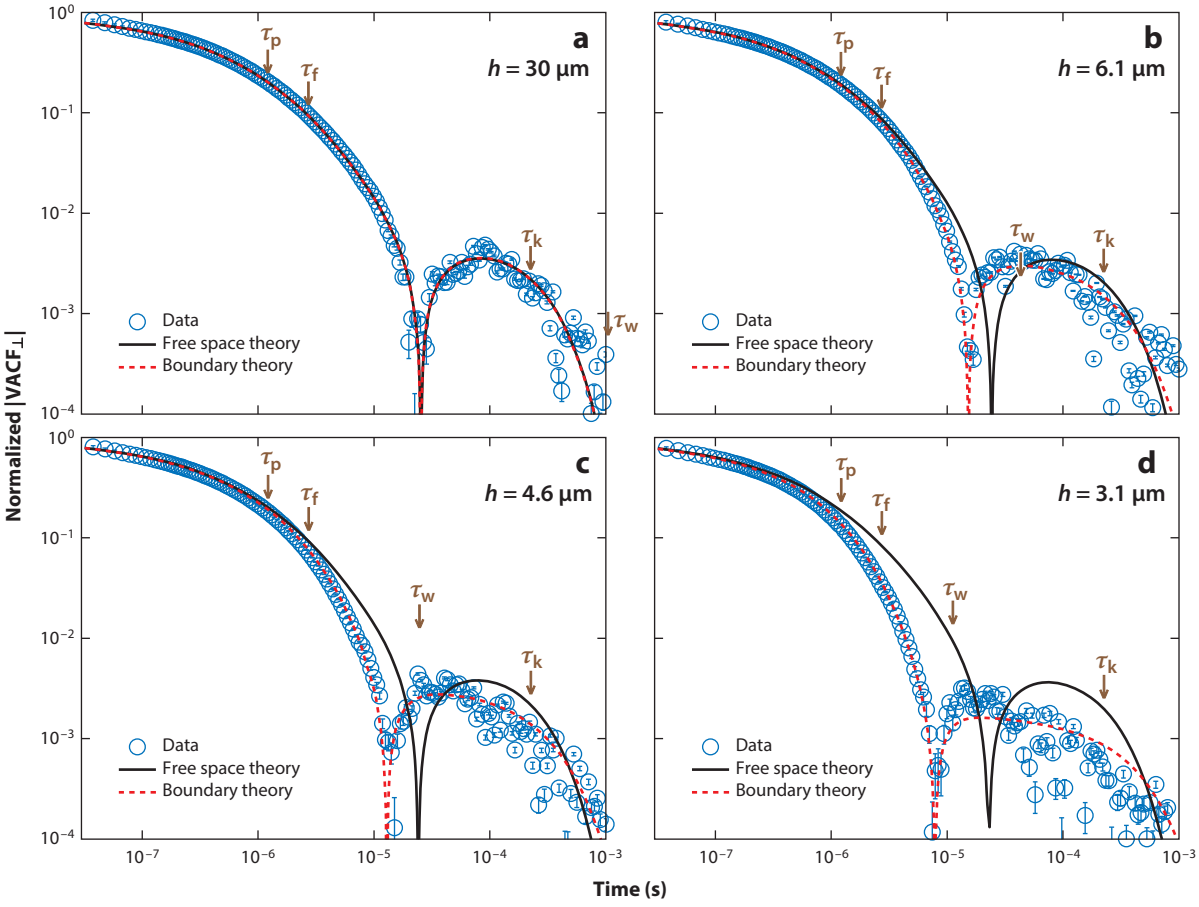


**Figure 7**

Experimental and theoretical velocity autocorrelation functions (VACFs) in the perpendicular direction at at four positions with respect to the wall, i.e., with a sphere–wall separation $h$ of 30 μm (*a*), 6.1 μm (*b*), 4.6 μm (*c*), and 3.1 μm (*d*). The panels show the absolute value, normalized to $\langle (v_\perp^*)^2 \rangle = k_B T / m_\perp^*$, on a log–log scale. The sharp, cusp-like features correspond to zero crossings. The blue circles are the experimental data, the black lines are the unbounded theoretical predictions (Clercx & Schram 1992), and the red dashed lines correspond to the bounded theoretical predictions at various sphere–wall separations (Mo et al. 2015b). There are four important timescales represented with brown arrows: $\tau_p = m_p/(6\pi\eta a^2) = (2\rho_p a^2)/(9\eta)$, the momentum relaxation time of the particle; $\tau_f = \rho_f a^2/\eta$, the timescale over which the vorticity diffuses over the size of the spherical particle; $\tau_w = h^2\rho_f/\eta$, the timescale over which the vorticity diffuses over the sphere–wall distance; and $\tau_k = \gamma(h)/K$, the trapping period. The VACF decays faster as the sphere approaches the wall.

More interestingly, the thermal force loses its color at low frequencies in the presence of a boundary. The FPSD acting on the particle near a no-slip wall becomes flat at low frequencies ($\omega\tau_f \ll 1$ and $\omega\tau_w \ll 1$, where $\tau_w$ is the time taken for vorticity in the fluid to traverse the distance from the wall to the sphere). This is believed to be a result of destructive interference between the incident and reflected flows, although more study is needed. The FPSDs in the direction perpendicular to the wall are shown in **Figure 8** for the same positions as in **Figure 7**. **Figure 8*a***, which has a large sphere–wall separation of $h = 30$ μm, shows that the boundary effects are negligible and verifies the colored thermal FPSD. **Figure 8*b–d*** shows that the FPSDs in the perpendicular direction flatten at low frequencies and that their DC ($f = 0$) values increase to

Annu. Rev. Fluid Mech. 2019.51:403-428. Downloaded from www.annualreviews.org
Access provided by University of Texas - Austin on 01/19/19. For personal use only.

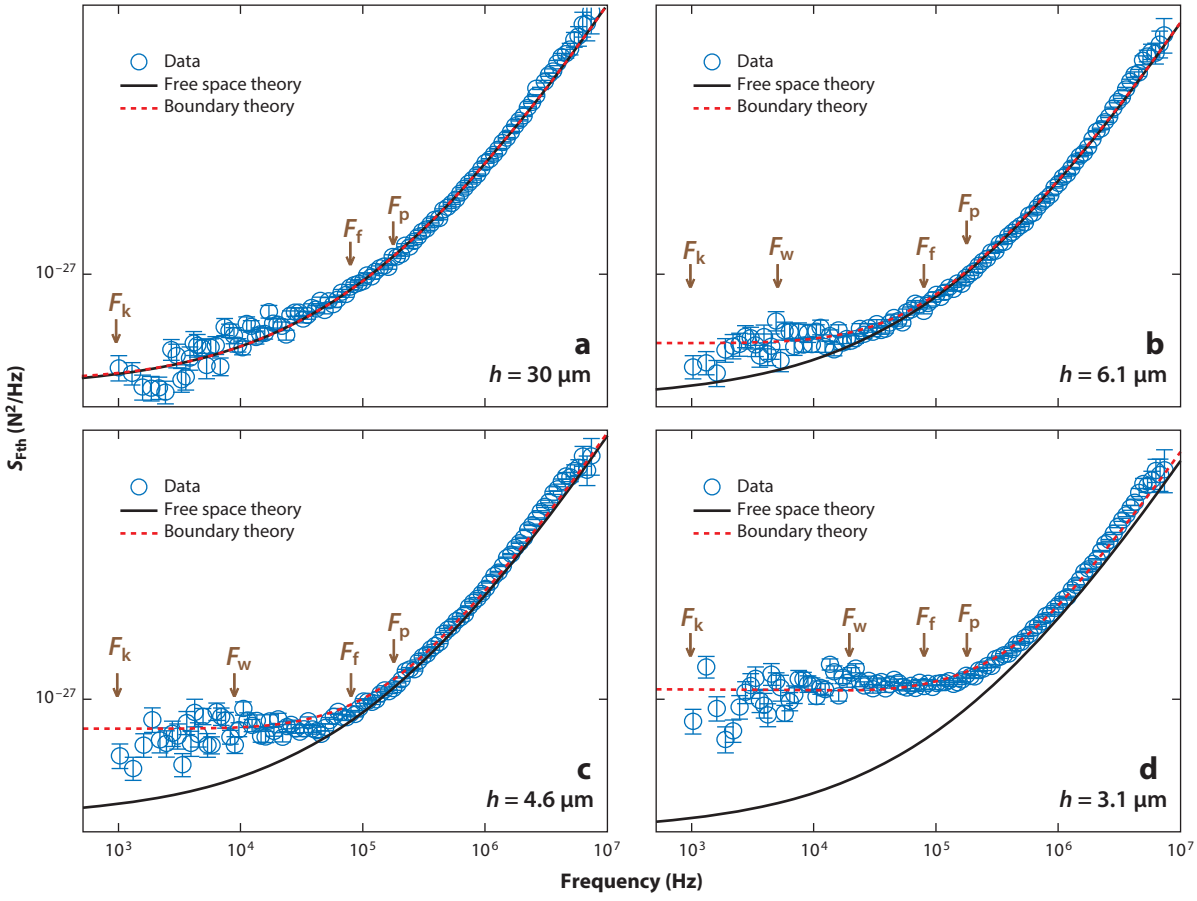


**Figure 8**

Experimental and theoretical thermal force power spectral density (FPSD) at the same positions as in **Figure 7** in the direction perpendicular to the wall: (*a*) $h = 30$ μm [$F_w = 1/(2\pi\tau_w) = 177$ Hz], (*b*) $h = 6.1$ μm [$F_w = 1/(2\pi\tau_w) = 4.3$ kHz], (*c*) $h = 4.6$ μm [$F_w = 1/(2\pi\tau_w) = 7.5$ kHz], and (*d*) $h = 3.1$ μm [$F_w = 1/(2\pi\tau_w) = 16.6$ kHz]. The blue circles are the experimental data [$F_p = 1/(2\pi\tau_p) = 153$ kHz, $F_f = 1/(2\pi\tau_f) = 68$ kHz, and $F_K = 1/(2\pi\tau_K) = 833$ Hz, where $\tau_K$ is the trapping period], the black lines are the unbounded theoretical predictions, and the red dashed lines correspond to the bounded theoretical predictions at various sphere–wall separations (Simha et al. 2018).

$4k_BT\gamma_s(1-\frac{9a}{8h})^{-1}$ from the bulk value of $4k_BT\gamma_s$. The increase in the thermal force is consistent with the increase in the drag force, in accordance with the fluctuation–dissipation theorem (Kubo 1966).

It is worth noting that this flattening of the FPSD explains the suppression of a resonance in the position power spectral density (PSD) of a particle near a wall that was observed but unexplained in previous experiments (Franosch et al. 2011, Jannasch et al. 2011). The resonance in position PSD is due to the color of the thermal force. The flattening in the thermal FPSD at low frequencies, caused by boundary effects, fades the thermal force's color and thus results in the suppression of the resonance in the position PSD. With small-enough sphere–wall separations, this resonance would disappear.

We provided a comprehensive study of boundary effects on Brownian motion over a wide range of timescales, in both the diffusive and the deep ballistic regime (Mo et al. 2015b, Simha

et al. 2018). We reported high-bandwidth, comprehensive measurements of Brownian motion of an optically trapped micrometer-sized silica sphere in water near an approximately flat wall. At short distances, we observed anisotropic Brownian motion with respect to the wall. We found that surface confinement occurs not only in the long-timescale diffusive regime but also in the short-timescale ballistic regime and that the VACF of the Brownian particle decays faster than that of a particle in bulk fluid. Furthermore, at low frequencies the thermal force loses its color due to the reflected flow from the no-slip boundary. A Brownian particle located near a flat wall provides a model system to study the behavior of more complex systems whose boundaries can be modeled as effective walls, such as blood vessels, cell membranes, and a variety of microfluidic geometries. This detailed understanding of boundary effects might enable the development of a new 3D microscope with a fast remote sensor to map out boundary contours (Mo et al. 2015b).

Annu. Rev. Fluid Mech. 2019.51:403-428. Downloaded from www.annualreviews.org
Access provided by University of Texas - Austin on 01/19/19. For personal use only.

## 5. BROWNIAN MOTION WITH SLIP BOUNDARY CONDITIONS

The boundary condition for the flow velocity of a viscous fluid at the solid–fluid interface is conventionally taken to be no-slip, meaning that the fluid molecules at the solid surface stick to the solid perfectly and have no relative velocity with the solid. Our experiments have shown that this is a good assumption for the interfaces between water and glass, as well as acetone and glass (Mo et al. 2015a,b).

The slippage of a fluid on a solid surface can be characterized by the slip length $\delta$ or the contact angle $\theta_c$, which are generally related through $\delta = \delta_0[1 + \cos(\theta_c)]^{-2}$, where $\delta_0$ is an empirical quasi-universal length scale (Huang et al. 2008). When $\delta$ is much smaller than the dimensions of interest, the fluid flow boundary condition can be safely assumed to be no-slip. The contact angle between water and glass typically lies in the range from 25° to 29° (Batchelor 2000), resulting in a slip length of 0.1 nm. Therefore, the interface between water and micron-sized glass particles satisfies the no-slip boundary condition since the particle's size is about $10^4$ times larger than the slip length. However, the no-slip boundary condition assumption has failed in many situations (Zhu & Granick 2001, Choi et al. 2006, Joseph et al. 2006, Huang et al. 2008, Liang & Keblinski 2015). Partial-slip boundary conditions must be used when the slip length $\delta$ is comparable to the dimensions of interest. Various microscopic structures on the surface of the solid have been demonstrated to increase the effective slip length (Choi et al. 2006, Joseph et al. 2006).

In previous work (Mo et al. 2017), we studied the Brownian motion of a trapped particle in bulk fluid with no-slip, partial-slip, and perfect-slip boundary conditions, as well as the dynamic motion of a microsphere with a no-slip boundary condition near a perfect-slip flat infinite wall and a no-slip flat infinite wall. Wettability has a direct bearing on the drag experienced by a particle in a liquid, which in turn has a measurable impact on its Brownian motion.

### 5.1. Brownian Motion of a Sphere in Bulk Fluid with Partial-Slip Boundary Condition

**Figure 9** shows the numerical predictions for the VACF (normalized to $k_B T/m^*$) of a trapped (150 μN/m) spherical particle (with diameter 3 μm and density 2 g/cm$^3$) with different boundary conditions on the sphere's surface in a fluid with density $\rho_f = 1$ g/cm$^3$ and dynamic viscosity $\eta = 0.9 \times 10^{-3}$ Pa·s. In particular, the agreement between the VACF with no-slip boundary condition and the VACF with a slip length of 0.1 nm indicates that the interface between glass and water indeed can be assumed to be no-slip in experiments (Mo et al. 2015a,b). With larger slip length, the particle VACF decays less rapidly over time, owing to a lower dissipation rate. Measurements of the particle's instantaneous velocity are of great significance to test the tenets of

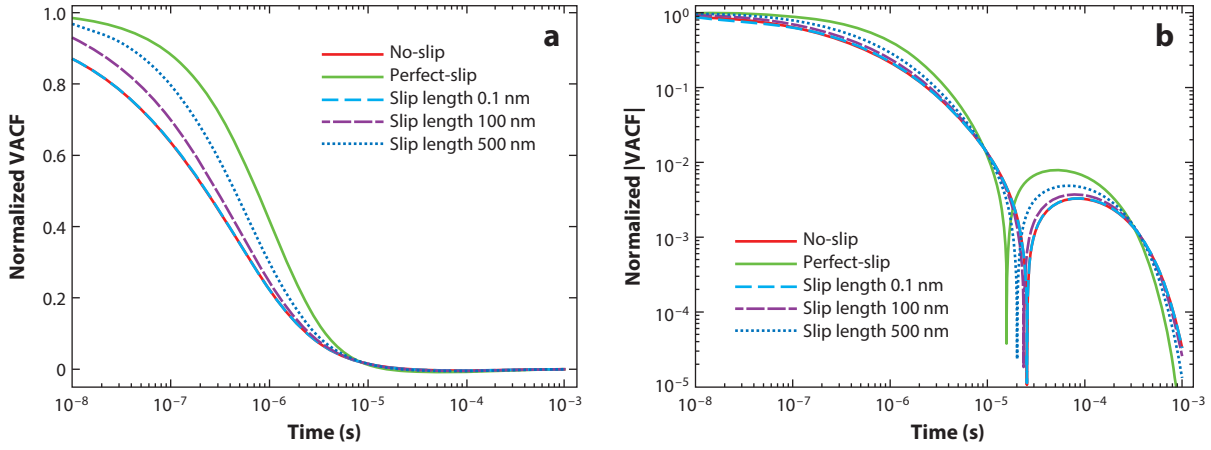


**Figure 9**

The numerical predictions for the velocity autocorrelation functions (normalized to $k_B T/m^*$) of an unbounded microsphere (with diameter 3 μm and density 2 g/cm$^3$) in a fluid with density $\rho_f = 1$ g/cm$^3$ and dynamic viscosity $\eta = 0.9 \times 10^{-3}$ Pa·s with different surface wettability conditions. Panel *a* gives the predictions on a log–linear plot, and panel *b* gives the absolute values on a log–log scale. The cusps indicate zero crossings, which are a consequence of the presence of the harmonic trap (150 μN/m). Figure adapted with permission from Mo et al. (2017).

Annu. Rev. Fluid Mech. 2019.51:403-428. Downloaded from www.annualreviews.org
Access provided by University of Texas - Austin on 01/19/19. For personal use only.

statistical mechanics, such as the MBD, as discussed in Section 3. To measure the instantaneous velocity of the particle, one needs to have a detection system with a temporal resolution high enough to measure the normalized VACF close to 1. Therefore, it is much easier to measure the instantaneous velocity of a particle with a perfect-slip boundary than with a no-slip boundary.

## 5.2. Brownian Motion of a No-Slip Sphere Near a Perfect-Slip Flat Wall

In Section 4, we have discussed the boundary effects on Brownian motion of a sphere imposed by a no-slip infinite flat wall and a no-slip cylindrical wall. In this section, we will discuss the boundary effects on Brownian motion of a microsphere imposed by a perfect-slip infinite flat wall. It is worth emphasizing that the sphere has the no-slip boundary condition. Readers are referred to Mo et al. (2017) for the detailed theory for such a system.

The MSD numerical predictions of the sphere in the three cases are shown in **Figure 10**. At long timescales, the MSDs of each case in both parallel and perpendicular directions plateau to the same value due to confinement caused by the harmonic trap (150 μN/m). As compared to the MSD of an unbounded particle, the MSDs in the perpendicular direction of the particle near both no-slip and perfect-slip walls are suppressed, meaning that the sphere experiences a stronger drag force when moving perpendicularly to the wall regardless of the boundary condition on the wall surface. However, the magnitude of the drag force depends on the boundary condition at the wall. In addition to this quantitative dependence on boundary conditions, the drag force on the sphere moving parallel to the wall has a qualitative dependence on the boundary conditions. It is surprising that in the parallel direction, the MSD of the sphere near the perfect-slip wall actually increases as compared to that of an unbounded sphere, which means that the sphere experiences less drag force when moving parallel to a perfect-slip wall as compared to that of an unbounded sphere, which has been observed (Wang et al. 2009).

**Figure 11** shows the numerical prediction of the absolute VACF, normalized to $\langle (v_\parallel^*)^2 \rangle = k_B T/m_\parallel^*$ and $\langle (v_\perp^*)^2 \rangle = k_B T/m_\perp^*$ in the parallel and perpendicular directions, respectively, of a

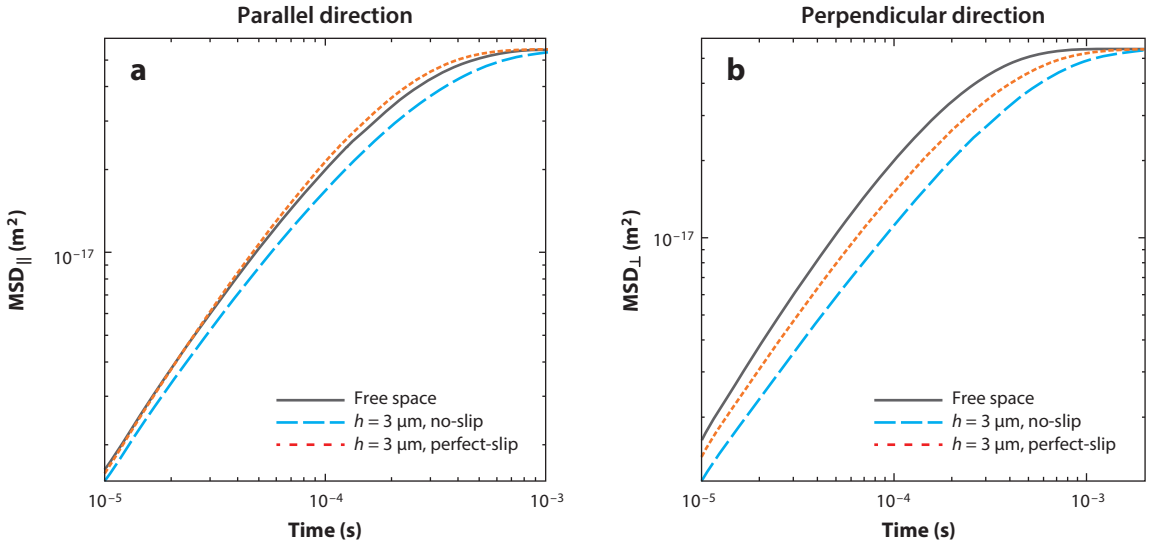


**Figure 10**

The numerical predictions of the mean square displacement (MSD) of a no-slip harmonically trapped (150 μN/m) microsphere (*a*) in the parallel direction and (*b*) in the perpendicular direction in three cases: unbounded, 3 μm away from a flat infinite no-slip wall, and 3 μm away from a flat infinite perfect-slip wall.

Annu. Rev. Fluid Mech. 2019.51:403-428. Downloaded from www.annualreviews.org
Access provided by University of Texas - Austin on 01/19/19. For personal use only.

harmonically trapped (150 μN/m) sphere in the three cases. In the perpendicular direction, the boundary effects imposed by both no-slip and perfect-slip walls cause a more rapid decay in VACF as compared to those in the bulk case. However, in the parallel direction, the VACF of a sphere near a perfect-slip wall first decays faster than the one in the bulk case, followed by slower decay at intermediate timescales.

## 6. BROWNIAN MOTION IN COMPRESSIBLE FLUIDS

We have observed that the velocity distribution of a microsphere in a liquid follows modified versions of the MBD and the energy equipartition theorem in Section 3. As discussed before, this is because the achieved temporal resolution, which is limited by the position sensitivity and ultimately by the shot noise of the detection beam, is not able to resolve the compressibility of the fluids (Mo et al. 2015a).

A simplified schematic of the experimental setup using pulsed laser probes to resolve compressibility of fluids is shown in **Figure 12**. The detection laser pulse is split into two pulses by polarization with controllable time delay $\tau_0$, which can be easily realized by adjusting the difference in optical path length between pulse 1 and pulse 2. In air, a 1-ns optical delay time corresponds to about 30 cm in optical path difference. Both $\tau_0$ and the laser pulse duration need to be shorter than $\tau_c$. The two probe pulses pass through a particle trapped by a continuous wave (CW) beam (not shown) with a time difference of $\tau_0$.

The positions of the particle $x(t_0)$ and $x(t_0 + \tau_0)$ can be obtained from detectors 1 and 2, respectively. With this, the position autocorrelation function at $\tau_0$, $C_x(\tau_0) = \langle x(t_0)x(t_0 + \tau_0)\rangle$, can be obtained experimentally by averaging many measurements with a fixed time delay $\tau_0$. By changing the optical path length difference, and thus $\tau_0$, one can get $C_x(\tau_0)$ over the entire time domain.

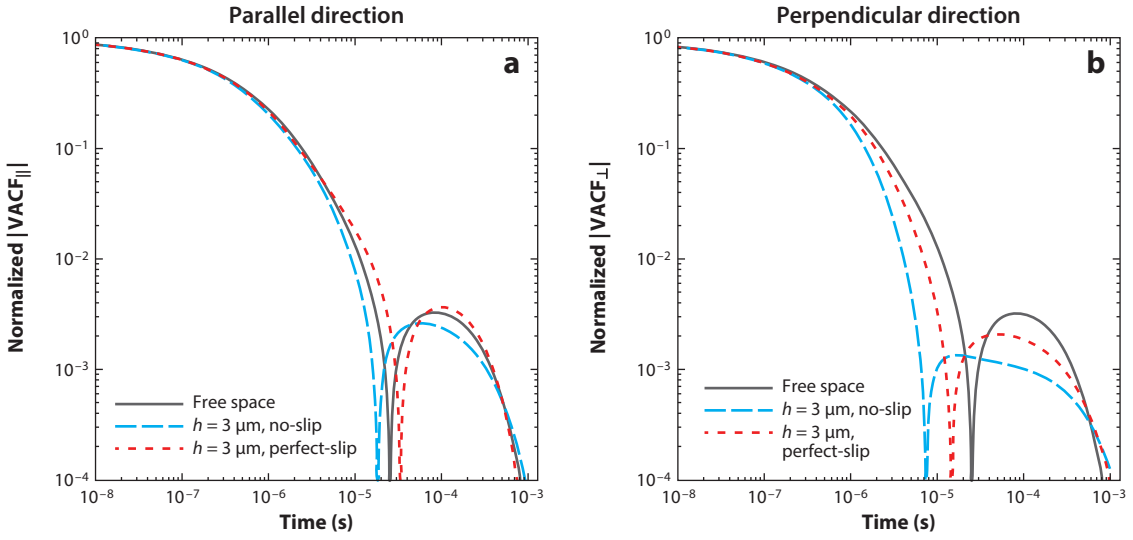


**Figure 11**

The numerical predictions of the velocity autocorrelation function (VACF) of a no-slip harmonically trapped (150 μN/m) microsphere (*a*) in the parallel direction and (*b*) in the pependicular direction in three cases: unbounded, 3 μm away from a flat infinite no-slip wall, and 3 μm away from a flat infinite perfect-slip wall. The panels show the absolute value, normalized to (*a*) $\langle (v_{\parallel}^{*})^2 \rangle = k_B T/m_{\parallel}^{*}$ and (*b*) $\langle (v_{\perp}^{*})^2 \rangle = k_B T/m_{\perp}^{*}$, on a log–log scale. The sharp, cusp-like features correspond to zero crossings.

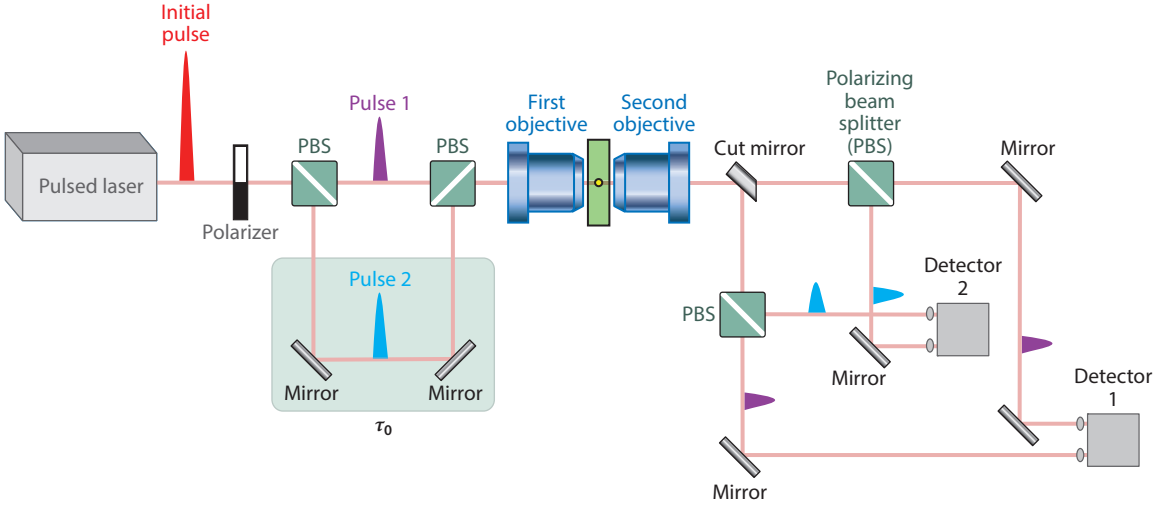


**Figure 12**

A simplified schematic of the experimental setup for studying Brownian motion using pulsed laser probes. The laser pulse is split by polarization into two pulses, pulse 1 (*purple*) and pulse 2 (*light blue*), with a controllable delay $\tau_0$. The two pulses pass through a microsphere trapped by a continuous wave beam (not shown) with time difference $\tau_0$ and incident onto two balanced detectors.

Annu. Rev. Fluid Mech. 2019.51:403-428. Downloaded from www.annualreviews.org
Access provided by University of Texas - Austin on 01/19/19. For personal use only.

The instantaneous velocity of the particle can be estimated using $v(t_0) = [x(t_0 + \tau_0) - x(t_0)]\tau_0$. The VACF can also be obtained by using four pulse probes instead of two.

In the presence of detection noise, the measured position of the microsphere by two detectors can be expressed as

$$x_{1,\mathrm{msr}}(t_0) = x_{1,\mathrm{s}}(t_0) + x_{1,\mathrm{n}}(t_0),\ x_{2,\mathrm{msr}}(t_0 + \tau_0) = x_{2,\mathrm{s}}(t_0 + \tau_0) + x_{2,\mathrm{n}}(t_0 + \tau_0), \quad 8.$$

where $x_{1,\mathrm{s}}(t_0)$ and $x_{1,\mathrm{n}}(t_0)$ are the real positions at time $t_0$ of the particle and the noise in the detection system 1, respectively, whereas $x_{2,\mathrm{s}}(t_0 + \tau_0)$ and $x_{2,\mathrm{n}}(t_0 + \tau_0)$ are the real positions at time $t_0 + \tau_0$ of the particle and the noise in the detection system 2, respectively. The instantaneous velocity of the trapped Brownian particle at time $t_0$ is given by

$$\begin{aligned} v_{\mathrm{s}}(t_0) &= \frac{x_{2,\mathrm{s}}(t_0 + \tau_0) - x_{1,\mathrm{s}}(t_0)}{\tau_0} \\ &= \frac{x_{2,\mathrm{msr}}(t_0 + \tau_0) - x_{1,\mathrm{msr}}(t_0)}{\tau_0} - \frac{x_{2,\mathrm{n}}(t_0 + \tau_0) - x_{1,\mathrm{n}}(t_0)}{\tau_0}. \end{aligned} \quad 9.$$

In general, $x_{1,\mathrm{n}}(t)$ and $x_{2,\mathrm{n}}(t)$ should behave similarly but will not be identical due to the two optical paths and the electronics in each system not being exactly the same, which will cause error in the instantaneous velocity measurement. As a result, it is necessary to calibrate the two detection systems. Active calibration was not needed using CW beam detection systems in our previous work (Mo et al. 2015a,b) because in a given data point the common classical noise, induced by the same optics and electronics, can be canceled by its adjacent data points with a 200-MHz sampling rate. At such high frequency, the shot noise dominates the classical noise, and the instantaneous velocity measurement is immune to low-frequency classical noise.

However, unlike the CW beam detection mode, which has passive calibration, in pulsed detection mode, one has to actively calibrate the two different detection systems. Calibration can be done by introducing a calibration pulse passing through the trapped particle and incident onto both detectors shortly before (or after) the probe pulses. As shown in **Figure 13**, after passing though the trapped particle $\delta t$ later than pulse 1, the unpolarized calibration pulse is split into two subpulses. The two detection systems can be calibrated as follows. The position measured by the two detection systems can be expressed as

$$x_{1,\mathrm{cali,msr}}(t_0 + \delta t) = x_{1,\mathrm{s}}(t_0 + \delta t) + x_{1,\mathrm{n}}(t_0 + \delta t), \quad 10.$$

$$x_{2,\mathrm{cali,msr}}(t_0 + \delta t) = x_{2,\mathrm{s}}(t_0 + \delta t) + x_{2,\mathrm{n}}(t_0 + \delta t). \quad 11.$$

Since the position of the Brownian particle measured by the two detection systems at the same time $t_0 + \delta t$ should be the same, namely, $x_{1,\mathrm{s}}(t_0 + \delta t) = x_{2,\mathrm{s}}(t_0 + \delta t)$, the relative noise difference between two detection systems at time $t_0 + \delta t$ can be calculated:

$$x_{1,\mathrm{n}}(t_0 + \delta t) - x_{2,\mathrm{n}}(t_0 + \delta t) = x_{1,\mathrm{cali,msr}}(t_0 + \delta t) - x_{2,\mathrm{cali,msr}}(t_0 + \delta t). \quad 12.$$

If both $\tau_0$ and $\delta t$ are much shorter than 1 μs, the differences among $x_{1,\mathrm{n}}(t_0)$, $x_{1,\mathrm{n}}(t_0 + \tau_0)$, and $x_{1,\mathrm{n}}(t_0 + \delta t + \tau_0)$ and among $x_{2,\mathrm{n}}(t_0)$, $x_{2,\mathrm{n}}(t_0 + \tau_0)$, and $x_{2,\mathrm{n}}(t_0 + \delta t + \tau_0)$ are small and dominated by shot noise. The instantaneous velocity of the trapped Brownian particle at time $t_0$ can be estimated as

$$v_{\mathrm{s}}(t_0) = \frac{x_{2,\mathrm{s}}(t_0 + \tau_0) - x_{1,\mathrm{s}}(t_0)}{\tau_0} \quad 13.$$

$$= \frac{x_{2,\mathrm{msr}}(t_0 + \tau_0) - x_{1,\mathrm{msr}}(t_0)}{\tau_0} - \frac{x_{2,\mathrm{n}}(t_0 + \tau_0) - x_{1,\mathrm{n}}(t_0)}{\tau_0} \quad 14.$$

$$= \frac{x_{2,\mathrm{msr}}(t_0 + \tau_0) - x_{1,\mathrm{msr}}(t_0)}{\tau_0} - \frac{x_{2,\mathrm{cali,msr}}(t_0 + \delta t) - x_{1,\mathrm{cali,msr}}(t_0 + \delta t)}{\tau_0}. \quad 15.$$



Annu. Rev. Fluid Mech. 2019.51:403-428. Downloaded from www.annualreviews.org
Access provided by University of Texas - Austin on 01/19/19. For personal use only.

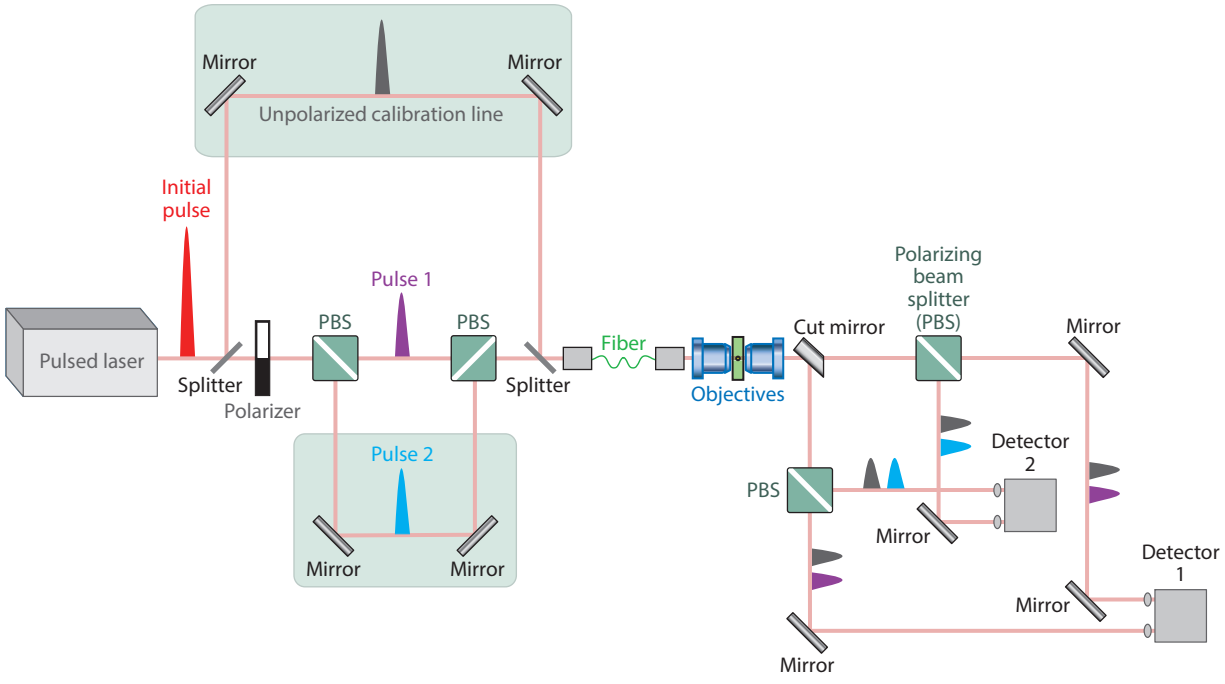


**Figure 13**

The simplified schematic for instantaneous velocity measurements of a Brownian particle using probe pulses with calibration. An unpolarized calibration pulse (*gray*) passes through the trapped microsphere $\delta t$ later than the pulse 1 (*purple*), and then is split into two subpulses going to the two respective detectors. A single-mode optical fiber is used to ensure that the probe and calibration pulses have the same optical path incident on the particle.

We can now measure the instantaneous velocity in the pulsed detection mode since every term in Equation 15 is measurable. This calibration using a CW laser beam can be understood in a similar way. It is important to note that the probe pulses and calibration pulse need to be temporally well resolved by the detectors. A single-mode fiber is needed to ensure that the probe pulses and calibration pulse have the same optical path incident on the trapped particle. The laser pulse intensity should be limited so as to not disturb the particle's motion, cause dielectric breakdown of the fluids, or temporally saturate photodiodes.

## 7. NONEQUILIBRIUM PHYSICS STUDY

In Langevin's model, there is a rapidly varying force constantly exerted on the particles in a fluid by the fluid molecules, which is often called thermal force and can drive even those particles with zero initial velocity to move. The thermal force is a white noise in gases, while a colored noise in liquids is due to the addition of the Basset force (Clercx & Schram 1992). The MSD has a $t^3$-dependence on time for a particle in a gas under the condition that the initial velocity is fixed rather than distributed thermally (Duplat et al. 2013). This observation is direct proof of the thermal force imagined by Langevin.

The ability to measure the instantaneous velocity of a Brownian particle will allow direct access to statistics of the energy and entropy exchange between the particle and the fluid, in both equilibrium and nonequilibrium experiments. As a model tool, Brownian motion has been used



Annu. Rev. Fluid Mech. 2019.51:403-428. Downloaded from www.annualreviews.org
Access provided by University of Texas - Austin on 01/19/19. For personal use only.

to study nonequilibrium physics in many studies (Kubo 1986, Katayama & Terauti 1999, Wang et al. 2002, D'Anna et al. 2003, Blickle et al. 2007, Imparato et al. 2007, Speck et al. 2007, Rings et al. 2010, Orihara & Takikawa 2011, Lindballe et al. 2013, Falasco et al. 2014).

Trapped gold nanospheres exhibit hot Brownian motion due to strong absorption of laser beams (Hajizadeh & Reihani 2010, Rings et al. 2010, Joly et al. 2011, Falasco et al. 2014). Hot Brownian motion deviates from the predictions of equilibrium Brownian motion because there is constant energy flow from the microsphere to the fluid. It is much easier to measure the motion of a gold particle than that of a dielectric sphere of the same size. This is because gold is much more dense, resulting in a longer momentum relaxation time $\tau_p$, and because gold nanospheres have much stronger scattering, resulting in higher optical gain and thus lower shot noise.

Another nonequilibrium situation can be created by moving hosting fluids (Katayama & Terauti 1999, Orihara & Takikawa 2011), which can break the symmetry of the velocity distribution and of the velocity dynamics. We can easily apply a known-velocity fluid flow using a syringe pump while studying the motion of the trapped particle. The maximum flow rate is limited by the trapping strength, which can be estimated to be about 10 mm/s with our experimental conditions. The corresponding Reynolds number is about $10^{-2}$; thus, the linearized Navier–Stokes equation is still a good approximation.

Perhaps a more systematic and controllable experiment is to use an optical pushing force (exerted by a CW beam or a pulsed beam) to drive the particle away from equilibrium. A 71-nN optical kicking force (three orders of magnitude larger than typical trapping forces) on a microsphere exerted by a pulsed laser has been measured, resulting in an average displacement of 208 nm (Lindballe et al. 2013). However, the achieved temporal resolution (1 ms, much longer than $\tau_p$) was far from being able to resolve how the velocity of the sphere decays after the kicking. Interestingly, it has been predicted that the velocity decays in a quantum oscillation–like way in short timescales when the compressibility of the fluid becomes important (Felderhof 2005a), meaning that the velocity does not decrease monotonically; instead, it oscillates with some damping. If the fluid is sufficiently compressible and its bulk viscosity is sufficiently smaller than its shear viscosity, the velocity of the particle after being kicked can even change its direction.

We propose a pump–probe experiment, as shown in **Figure 14**, to study such interesting phenomena. Based on the pulsed probe experiment shown in **Figure 13**, a kicking pulse is introduced from the side by an optical fiber with a microlens on the tip. The kicking optical fiber can be easily integrated into the flow cell used in previous work (Kheifets et al. 2014; Mo et al. 2015a,b). The kicking pulse and probe pulses can originate from the same laser with a well-defined delay $\delta t$. By changing the delay time, one can measure how the particle momentum decays with time.

The measurement of the instantaneous velocity of a Brownian particle and the excellent agreement with the MBD imply that we now have a new, ultrasensitive analytical tool to weigh a particle in situ, where the mass is used as a fitting parameter. Aside from the added mass correction in a liquid, the ability to weigh a particle in real time does not seem very important when its mass does not change. However, the situation is drastically different for a test particle in a supersaturated vapor or in a supercooled liquid. In these cases, we propose that an optically trapped particle can be used as a new testing ground for heterogeneous nucleation. This problem is of central interest for understanding the transition from a supercooled liquid to a solid, which is especially relevant to the theory of glasses (Sosso et al. 2016). Beyond basic physics, nucleation in a supersaturated vapor is the mechanism for ice formation in clouds and hence of intense interest in atmospheric science (Hegg & Baker 2009). The long-standing dream of cloud seeding has never realized its potential due to the many parameters involved in nucleation. We propose that an optically trapped particle is an ideal test bed for optimizing nucleation as a function of material, size, surface chemistry, charge, and morphology. This combination of a new experimental system



Annu. Rev. Fluid Mech. 2019.51:403-428. Downloaded from www.annualreviews.org
Access provided by University of Texas - Austin on 01/19/19. For personal use only.

Annu. Rev. Fluid Mech. 2019.51:403-428. Downloaded from www.annualreviews.org
Access provided by University of Texas - Austin on 01/19/19. For personal use only.

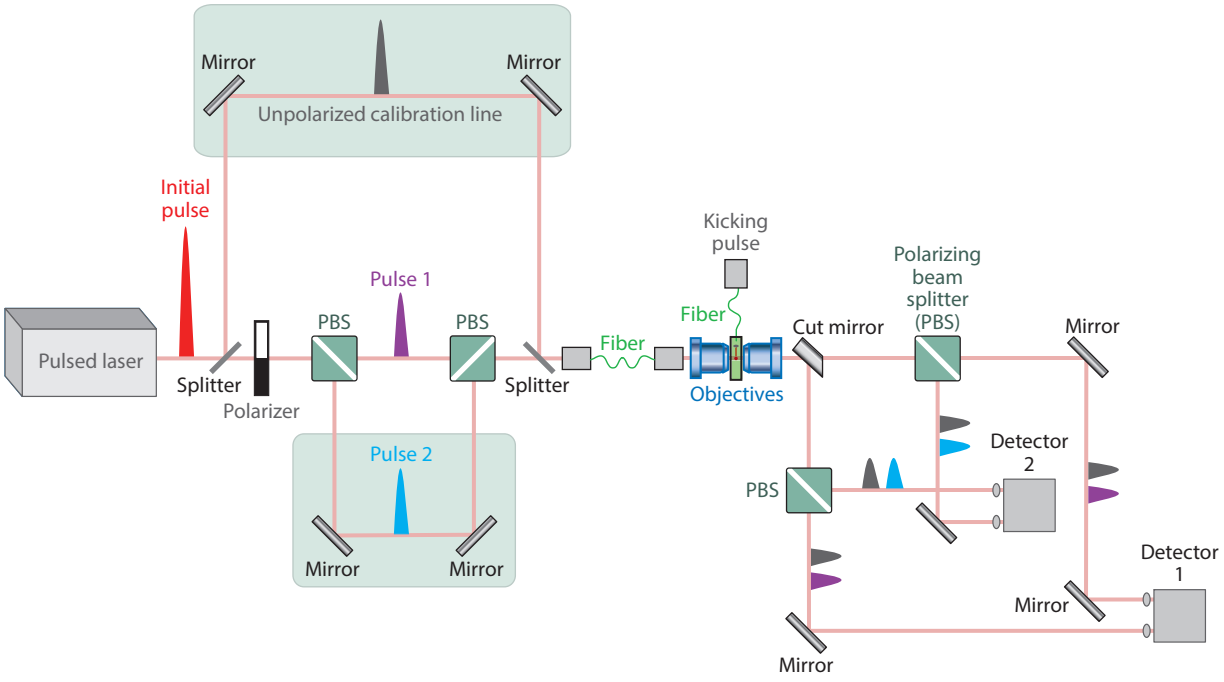


**Figure 14**

The simplified schematic of a pump–probe experiment based on the pulsed probe experiment shown in **Figure 13**. A kicking pulse is introduced by an optical fiber with a microlens on its tip. The probe pulses are delayed by $\delta t$ after the kicking pulse.

together with computational modeling has the potential for a breakthrough in the understanding of nucleation and for real-life applications to cloud seeding.

## DISCLOSURE STATEMENT

The authors are not aware of any biases that might be perceived as affecting the objectivity of this review.

## ACKNOWLEDGMENTS

We acknowledge support from the Sid W. Richardson Foundation and the R.A. Welch Foundation grant number F-1258.

## LITERATURE CITED

Alam MS, Ishii K, Hasimoto H. 1980. Slow motion of a small sphere outside of a circular cylinder. *J. Phys. Soc. Jpn.* 49:405–8

Alder BJ, Wainwright TE. 1967. Velocity autocorrelations for hard spheres. *Phys. Rev. Lett.* 18:988–90

Alder BJ, Wainwright TE. 1970. Decay of the velocity autocorrelation function. *Phys. Rev. A* 1:18–21

Ashkin A. 1970. Acceleration and trapping of particles by radiation pressure. *Phys. Rev. Lett.* 24:156–59

Ashkin A. 1992. Forces of a single-beam gradient laser trap on a dielectric sphere in the ray optics regime. *Biophys. J.* 61:569–82

Ashkin A. 2000. History of optical trapping and manipulation of small-neutral particle, atoms, and molecules. *IEEE J. Selected Top. Quantum Electron.* 6:841–56
Ashkin A, Dziedzic JM. 1975. Optical levitation of liquid drops by radiation pressure. *Science* 187:1073–75
Ashkin A, Dziedzic JM. 1976. Optical levitation in high vacuum. *Appl. Phys. Lett.* 28:333–35
Ashkin A, Dziedzic JM. 1987. Optical trapping and manipulation of viruses and bacteria. *Science* 235:1517–20
Ashkin A, Dziedzic JM, Bjorkholm JE, Chu S. 1986. Observation of a single-beam gradient force optical trap for dielectric particles. *Opt. Lett.* 11:288–90
Ashkin A, Dziedzic JM, Yamane T. 1987. Optical trapping and manipulation of single cells using infrared laser beams. *Nature* 330:769–71
Basset AB. 1888. On the motion of a sphere in a viscous liquid. *Philos. Trans. R. Soc. A* 179:43–63
Batchelor GK. 2000. *An Introduction to Fluid Dynamics*. Cambridge, UK: Cambridge Univ. Press
Blickle V, Speck T, Lutz C, Seifert U, Bechinger C. 2007. Einstein relation generalized to nonequilibrium. *Phys. Rev. Lett.* 98:210601
Boussinesq J. 1885. Sur la résistance qu'oppose un liquide indéfini en repos, sans pesanteur, au mouvement varié d'une sphère solide qu'il mouille sur toute sa surface, quand les vitesses restent bien continues et assez faibles pour que leurs carrés et produits soient négligeables. *C.R. Acad. Sci.* 100:935–37
Brown R. 1827. A brief account of microscopical observations made in the months of June, July and August, 1827, on the particles contained in the pollen of plants; and on the general existence of active molecules in organic and inorganic bodies. *Philos. Mag. Ser. 2* 4:161–73
Chavez I, Huang R, Henderson K, Florin EL, Raizen MG. 2008. Development of a fast position-sensitive laser beam detector. *Rev. Sci. Instrum.* 79:105104
Cheezum MK, Walker WF, Guilford WH. 2001. Quantitative comparison of algorithms for tracking single fluorescent particles. *Biophys. J.* 81:2378–88
Choi CH, Ulmanella U, Kim J, Ho CM, Kim CJ. 2006. Effective slip and friction reduction in nanograted superhydrophobic microchannels. *Phys. Fluids* 18:087105
Clayton DD. 1974. Maxwellian relative energies and solar neutrinos. *Nature* 249:131
Clercx H, Schram P. 1992. Brownian particles in shear flow and harmonic potentials: a study of long-time tails. *Phys. Rev. A* 46:1942–50
D'Anna G, Mayor P, Barrat A, Loreto V, Nori F. 2003. Observing Brownian motion in vibration-fluidized granular matter. *Nature* 424:909–12
Duplantier B. 2006. Brownian motion, "diverse and undulating." In *Einstein, 1905–2005: Poincaré Seminar 2005*, ed. T Damour, O Darrigol, B Duplantier, V Rivasseau, pp. 201–93. Basel, Switz.: Birkhäuser Verlag
Duplat J, Kheifets S, Li T, Raizen M, Villermaux E. 2013. Superdiffusive trajectories in Brownian motion. *Phys. Rev. E* 87:020105
Einstein A. 1905. Investigations on the theory of the Brownian movement. *Ann. Phys.* 322:549–60
Einstein A. 1907. Theoretische Bemerkungen über die Brownsche Bewegung. *Z. Elektrochem. Angew.* 13:41–42
Exner FM. 1900. Notiz zu Brown's Molecularbewegung. *Ann. Phys.* 307:843–47
Falasco G, Gnann MV, Rings D, Kroy K. 2014. Effective temperatures of hot Brownian motion. *Phys. Rev. E* 90:032131
Felderhof BU. 2005a. Backtracking of a sphere slowing down in a viscous compressible fluid. *J. Chem. Phys.* 123:044902
Felderhof BU. 2005b. Effect of the wall on the velocity autocorrelation function and long-time tail of Brownian motion. *J. Phys. Chem. B* 109:21406–12
Franosch T, Grimm M, Belushkin M, Mor FM, Foffi G, et al. 2011. Resonances arising from hydrodynamic memory in Brownian motion. *Nature* 478:85–88
Franosch T, Jeney S. 2009. Persistent correlation of constrained colloidal motion. *Phys. Rev. E* 79:031402
Gittes F, Schmidt CF. 1998. Interference model for back-focal-plane displacement detection in optical tweezers. *Opt. Lett.* 23:7–9
Gotoh T, Kaneda Y. 1981. Effect of an infinite plane wall on the motion of a spherical. *J. Chem. Phys.* 76:3193–97
Gould RJ. 1971. Deviation from a Maxwellian velocity distribution in low-density plasmas. *Phys. Fluids* 14:1701–6

Annu. Rev. Fluid Mech. 2019.51:403-428. Downloaded from www.annualreviews.org
Access provided by University of Texas - Austin on 01/19/19. For personal use only.

Gould RJ, Levy M. 1976. Deviation from a Maxwellian velocity distribution in regions of interstellar molecular hydrogen. *Astrophys. J.* 206:435–39
Grimm M, Jeney S, Franosch T. 2011. Brownian motion in a Maxwell fluid. *Soft Matter* 7:2076–84
Hajizadeh F, Reihani SNS. 2010. Optimized optical trapping of gold nanoparticles. *Opt. Express* 18:551–59
Hammond AP, Corwin EI. 2017. Direct measurement of the ballistic motion of a freely floating colloid in Newtonian and viscoelastic fluids. *Phys. Rev. E* 96:042606
Han Y, Alsayed AM, Nobili M, Zhang J, Lubensky TC, Yodh AG. 2006. Brownian motion of an ellipsoid. *Science* 314:626–30
Happel J, Brenner H. 1983. *Low Reynolds Number Hydrodynamics: With Special Applications to Particulate Media*. The Hague, Neth.: Martinus Nijhoff
Harada Y, Asakura T. 1996. Radiation forces on a dielectric sphere in the Rayleigh scattering regime. *Opt. Commun.* 124:529–41
Hegg DA, Baker MB. 2009. Nucleation in the atmosphere. *Rep. Progress Phys.* 72:056801
Hinch EJ. 1975. Application of the Langevin equation to fluid suspensions. *J. Fluid Mech.* 72:499–511
Huang DM, Sendner C, Horinek D, Netz RR, Bocquet L. 2008. Water slippage versus contact angle: a quasiuniversal relationship. *Phys. Rev. Lett.* 101:226101
Huang K. 1987. *Statistical Mechanics*. Hoboken, NJ: Wiley. 2nd ed.
Huang K, Szlufarska I. 2015. Effect of interfaces on the nearby Brownian motion. *Nat. Commun.* 6:8558
Imparato A, Peliti L, Pesce G, Rusciano G, Sasso A. 2007. Work and heat probability distribution of an optically driven Brownian particle: theory and experiments. *Phys. Rev. E* 76:050101
Jannasch A, Mahamdeh M, Schäffer E. 2011. Inertial effects of a small Brownian particle cause a colored power spectral density of thermal noise. *Phys. Rev. Lett.* 107:228301
Jeney S, Lukić B, Kraus JA, Franosch T, Forró L. 2008. Anisotropic memory effects in confined colloidal diffusion. *Phys. Rev. Lett.* 100:240604
Joly L, Merabia S, Barrat JL. 2011. Effective temperatures of a heated Brownian particle. *Europhys. Lett.* 94:50007
Joseph P, Cottin-Bizonne C, Benoît JM, Ybert C, Journet C, et al. 2006. Slippage of water past superhydrophobic carbon nanotube forests in microchannels. *Phys. Rev. Lett.* 97:156104
Kalmykov YP, Coffey WT. 2017. *The Langevin Equation: With Applications in Physics, Chemistry and Electrical Engineering*. Singapore: World Sci. 4th ed.
Katayama Y, Terauti R. 1999. Brownian motion of a single particle under shear flow. *Eur. J. Phys.* 17:136–40
Keen S, Leach J, Gibson G, Padgett MJ. 2007. Comparison of a high-speed camera and a quadrant detector for measuring displacements in optical tweezers. *J. Opt. A* 9:S264–66
Kelvin L. 1892. On a decisive test-case disproving the Maxwell-Boltzmann doctrine regarding distribution of kinetic energy. *Proc. R. Soc. Lond.* 51:397–99
Kerker M. 1974. Brownian movement and molecular reality prior to 1900. *J. Chem. Educ.* 51:764–68
Kheifets S, Simha A, Melin K, Li T, Raizen MG. 2014. Observation of Brownian motion in liquids at short times: instantaneous velocity and memory loss. *Science* 343:1493–96
Klafter J, Shlesinger MF, Zumofen G. 1996. Beyond Brownian motion. *Phys. Today* 49:33–39
Kubo R. 1966. Fluctuation-dissipation theorem. *Rep. Prog. Phys.* 29:255–84
Kubo R. 1986. Brownian motion and nonequilibrium statistical mechanics. *Science* 233:330–34
Langevin P. 1908. Sur la théorie cinétique du mouvement Brownien. *C.R. Acad. Sci.* 146:530–33
Lemons DS, Gythiel A. 1997. Paul Langevin's 1908 paper "On the theory of Brownian motion." *Am. J. Phys.* 65:1079–81
Li T. 2011. *Fundamental tests of physics with optically trapped microspheres*. PhD Thesis, Univ. Texas at Austin
Li T, Kheifets S, Medellin D, Raizen MG. 2010. Measurement of the instantaneous velocity of a Brownian particle. *Science* 328:1673–75
Liang Z, Keblinski P. 2015. Slip length crossover on a graphene surface. *J. Chem. Phys.* 142:134701
Lindballe TB, Kristensen MVG, Berg-Sørensen K, Keiding SR, Stapelfeldt H. 2013. Pulsed laser manipulation of an optically trapped bead: averaging thermal noise and measuring the pulsed force amplitude. *Opt. Express* 21:1986–96
Liu L, Woolf A, Rodriguez AW, Capasso F. 2014. Absolute position total internal reflection microscopy with an optical tweezer. *PNAS* 111:E5609–15

Annu. Rev. Fluid Mech. 2019.51:403-428. Downloaded from www.annualreviews.org
Access provided by University of Texas - Austin on 01/19/19. For personal use only.

Lorentz H. 1907. *Abhandlungen über theoretische Physik*. Leipzig, Ger.: Teubner Verlag
Lukic B, Jeney S, Tischer C, Kulik AJ, Forro L, et al. 2005. Direct observation of nondiffusive motion of a Brownian particle. *Phys. Rev. Lett.* 95:160601
Mo J. 2015. *Short timescale Brownian motion and applications*. PhD Thesis, Univ. Texas at Austin
Mo J, Simha A, Kheifets S, Raizen MG. 2015a. Testing the Maxwell-Boltzmann distribution using Brownian particles. *Opt. Express* 23:1888–93
Mo J, Simha A, Raizen MG. 2015b. Broadband boundary effects on Brownian motion. *Phys. Rev. E* 92:062106
Mo J, Simha A, Raizen MG. 2017. Brownian motion as a new probe of wettability. *J. Chem. Phys.* 146:134707
Nieminen TA, Loke VLY, Stilgoe AB, Knöner G, Brańczyk AM, et al. 2007. Optical tweezers computational toolbox. *J. Opt. A* 9:S196–203
Orihara H, Takikawa Y. 2011. Brownian motion in shear flow: direct observation of anomalous diffusion. *Phys. Rev. E* 84:061120
Parthasarathy R. 2012. Rapid, accurate particle tracking by calculation of radial symmetry centers. *Nat. Methods* 9:724–26
Perrin J. 1909. Brownian movement and molecular reality. *Ann. Chim. Phys.* 18:1–116
Pomeau Y, Piasecki J. 2017. L'équation de Langevin. *C.R. Acad. Sci.* 146:530–33
Pralle A, Prummer M, Florin EL, Stelzer EH, Hörber JK. 1999. Three-dimensional high-resolution particle tracking for optical tweezers by forward scattered light. *Microsc. Res. Tech.* 44:378–86
Rahman A. 1964. Correlations in the motion of atoms in liquid argon. *Phys. Rev.* 136:405–11
Rahman A. 1966. Liquid structure and self-diffusion. *J. Chem. Phys.* 45:2585–92
Rings D, Schachoff R, Selmke M, Cichos F, Kroy K. 2010. Hot Brownian motion. *Phys. Rev. Lett.* 105:090604
Simha A, Mo J, Morrison PJ. 2018. On the point-particle approximation for the unsteady Stokes equations. *J. Fluid Mech.* In press
Sosso GC, Chen J, Cox SJ, Fitzner M, Pedevilla P, et al. 2016. Crystal nucleation in liquids: open questions and future challenges in molecular dynamics simulations. *Chem. Rev.* 116:7078–116
Speck T, Blickle V, Bechinger C, Seifert U. 2007. Distribution of entropy production for a colloidal particle in a nonequilibrium steady state. *Europhys. Lett.* 79:30002
Stokes GG. 1850. On the effect of the internal friction of fluids on the motion of pendulums. *Trans. Cambr. Philos. Soc.* 9:8–106
Tatsumi R, Yamamoto R. 2013. Propagation of hydrodynamic interactions between particles in a compressible fluid. *Phys. Fluids* 25:046101
Tolic-Norrelykke SF, Schaffer E, Howard J, Pavone FS, Julicher F, Flyvbjerg H. 2006. Calibration of optical tweezers with positional detection in the back focal plane. *Rev. Sci. Instrum.* 77:103101
Uhlenbeck GE, Ornstein LS. 1930. On the theory of the Brownian motion. *Phys. Rev.* 36:823–41
Vicsek T. 1992. *Fractal Growth Phenomena*. Singapore: World Sci.
von Smoluchowski M. 1906. Zur kinetischen Theorie der Brownschen Molekularbewegung und der Suspensionen. *Ann. Phys.* 326:756–80
Wakiya S. 1964. Effect of a plane wall on the impulse motion of a sphere in a viscous fluid. *J. Phys. Soc. Jpn.* 19:1401–8
Waleed M, Madsen L, Casacio CA, Taylor MA, Mauranyapin NP, Bowen WP. 2017. *High bandwidth optical tracking of micro/nanoparticles*. Paper presented at Optical Trappings and Optical Micromanipulation XIV, San Diego, CA, 9 Aug.
Wang GM, Prabhakar R, Sevick EM. 2009. Hydrodynamic mobility of an optically trapped colloidal particle near fluid-fluid interfaces. *Phys. Rev. Lett.* 103:248303
Wang GM, Sevick EM, Mittag E, Searles DJ, Evans DJ. 2002. Experimental demonstration of violations of the second law of thermodynamics for small systems and short time scales. *Phys. Rev. Lett.* 89:50601
Widom A. 1971. Velocity fluctuations of a hard-core Brownian particle. *Phys. Rev. A* 3:1394–96
Yang FL. 2010. A formula for the wall-amplified added mass coefficient for a solid sphere in normal approach to a wall and its application for such motion at low Reynolds number. *Phys. Fluids* 22:123303
Yu HY, Eckmann DM, Ayyaswamy PS, Radhakrishnan R. 2015. Composite generalized Langevin equation for Brownian motion in different hydrodynamic and adhesion regimes. *Phys. Rev. E* 91:052303
Zhu Y, Granick S. 2001. Rate-dependent slip of Newtonian liquid at smooth surfaces. *Phys. Rev. Lett.* 87:096105
Zwanzig R, Bixon M. 1970. Hydrodynamic theory of the velocity correlation function. *Phys. Rev. A* 2:2005–12
Zwanzig R, Bixon M. 1975. Compressibility effects in the hydrodynamic theory of Brownian motion. *J. Fluid Mech.* 69:21–25

Annu. Rev. Fluid Mech. 2019.51:403-428. Downloaded from www.annualreviews.org
Access provided by University of Texas - Austin on 01/19/19. For personal use only.

Annual Review of
Fluid Mechanics

Volume 51, 2019

# Contents



Annu. Rev. Fluid Mech. 2019.51:403-428. Downloaded from www.annualreviews.org
Access provided by University of Texas - Austin on 01/19/19. For personal use only.

**Indexes**



**Errata**

An online log of corrections to *Annual Review of Fluid Mechanics* articles may be found at http://www.annualreviews.org/errata/fluid

Annu. Rev. Fluid Mech. 2019.51:403-428. Downloaded from www.annualreviews.org
Access provided by University of Texas - Austin on 01/19/19. For personal use only.